

Article

# Estimating Forest Structural Parameters Using Canopy Metrics Derived from Airborne LiDAR Data in Subtropical Forests

Zhengan Zhang, Lin Cao \* and Guanghui She

Co-Innovation Center for Sustainable Forestry in Southern China, Nanjing Forestry University, Nanjing 210037, China; Zhangzhengnan\_njfu@hotmail.com (Z.Z.); ghshe@njfu.edu.cn (G.S.)

\* Correspondence: lincao@njfu.edu.cn

Received: 14 June 2017; Accepted: 6 September 2017; Published: 11 September 2017

**Abstract:** Accurate and timely estimation of forest structural parameters plays a key role in the management of forest resources, as well as studies on the carbon cycle and biodiversity. Light Detection and Ranging (LiDAR) is a promising active remote sensing technology capable of providing highly accurate three dimensional and wall-to-wall forest structural characteristics. In this study, we evaluated the utility of standard metrics and canopy metrics derived from airborne LiDAR data for estimating plot-level forest structural parameters individually and in combination, over a subtropical forest in Yushan forest farm, southeastern China. Standard metrics, i.e., height-based and density-based metrics, and canopy metrics extracted from canopy vertical profiles, i.e., canopy volume profile (CVP), canopy height distribution (CHD), and foliage profile (FP), were extracted from LiDAR point clouds. Then the standard metrics and canopy metrics were used for estimating forest structural parameters individually and in combination by multiple regression models, including forest type-specific (coniferous forest, broad-leaved forest, mixed forest) models and general models. Additionally, the synergy of standard metrics and canopy metrics for estimating structural parameters was evaluated using field measured data. Finally, the sensitivity of vertical and horizontal resolution of voxel size for estimating forest structural parameters was assessed. The results showed that, in general, the accuracies of forest type-specific models ( $Adj-R^2 = 0.44-0.88$ ) were relatively higher than general models ( $Adj-R^2 = 0.39-0.77$ ). For forest structural parameters, the estimation accuracies of Lorey's mean height ( $Adj-R^2 = 0.61-0.88$ ) and aboveground biomass ( $Adj-R^2 = 0.54-0.81$ ) models were the highest, followed by volume ( $Adj-R^2 = 0.42-0.78$ ), DBH ( $Adj-R^2 = 0.48-0.74$ ), basal area ( $Adj-R^2 = 0.41-0.69$ ), whereas stem density ( $Adj-R^2 = 0.39-0.64$ ) models were relatively lower. The combination models ( $Adj-R^2 = 0.45-0.88$ ) had higher performance compared with models developed using standard metrics (only) ( $Adj-R^2 = 0.42-0.84$ ) and canopy metrics (only) ( $Adj-R^2 = 0.39-0.83$ ). The results also demonstrated that the optimal voxel size was  $5 \times 5 \times 0.5 \text{ m}^3$  for estimating most of the parameters. This study demonstrated that canopy metrics based on canopy vertical profiles can be effectively used to enhance the estimation accuracies of forest structural parameters in subtropical forests.

**Keywords:** forest structural parameter; LiDAR; canopy metric; canopy vertical profile; subtropical forest

## 1. Introduction

Forested ecosystems are spatially dynamic and continuously changing and therefore comprise complex and heterogeneous forest structures [1,2]. Forest structure, defined as the spatiotemporal arrangement of structural components in specific vertical and horizontal spatial patterns within a forest stand [3–5], is recognized as both a product and driver of forest biophysical processes [6]

and represents important forest information, which is useful for guiding multi-functional forest management [7]. Forest structural parameters (e.g., tree height, volume, biomass or stem density etc.) provide considerable information on the spatial and temporal distribution of forests as well as structural properties, and are considered critical components of forest inventory [8] and reliable diversity indicators across forest successional stages [3]. So obtaining spatially continuous estimates of forest structural parameters is valuable for supporting long-term sustainable forest management [9].

Subtropical forests are distributed in a transition zone between tropical and temperate zones, i.e., the region lying largely from 23.5° to 40° latitude in the northern or southern hemispheres [10]. Subtropical forests consist of both subtropical humid and subtropical dry forests, which have unique ecological characteristics when compared to tropical and temperate regions [11]. Subtropical forests, which account for approximately 9% of the world's forest area [12], are considered a carbon sink contributing to global forest carbon sequestration, and have high species richness, complex structure of forest, high biodiversity and high net ecosystem productivity (NEP) [11]. Quantitative measurements of forest structural parameters of subtropical forests are required to understand forest ecological mechanisms, promote regional ecological developments, maintain biodiversity and enhance regional carbon balance [13].

Traditionally, forest structural parameters are assessed by conventional field inventories, which is time-consuming, costly and limited in spatial extent [2,14]. As a promising earth observation technique, remote sensing has shown great potential for providing multi-scale, multi-dimensional and multi-temporal earth surface information [15] for instantaneous, quantificational and accurate measurements of spatially continuous wall-to-wall properties of forest structure over large-scale areas in lieu of time-consuming and labor-intensive inventory [16]. Furthermore, integrating information from remotely sensed data with a high level of precision and temporal consistency has been recognized as having the ability to describe forest biophysical properties and effectively enhance the performance of forest structure estimations [17].

Estimates of forest stand structural parameters have been derived from optical remote sensing data for several decades [17,18]. However, passive remote signals are generally reflected or absorbed in the uppermost canopy layers and tend to “saturate”, especially in dense forest (i.e., high canopy closure), limiting the ability to characterize vertical structure [19,20]. Similarly, Radar (Radio Detection and Ranging) technology also reveals the aforementioned data saturation problems, due to noise introduced by terrain, surface moisture and other factors [20,21]. Conversely, as a promising active remote sensing technology, Light Detection and Ranging (LiDAR) can be used to directly estimate a spatially explicit three-dimensional (3D) canopy structure with submeter accuracy by transmitting short laser pulses and receiving returned signals [22,23]. Furthermore, LiDAR systems have the ability to overcome the data saturation problems in optical or Radar remote sensing, as a laser beam can strongly penetrate through even dense and multilayered forest canopies to the earth's surface [24].

Means et al. (2000) [25] estimated forest structural parameters, i.e., tree height, basal area, and volume, using airborne LiDAR data over a Douglas-fir-dominated temperate forest in the Western Cascades of Oregon. They found that the estimation of tree height predicted by the metrics of height percentiles and resulted in  $R^2$  values of 0.93–0.98. The  $R^2$  values were 0.94–0.95 and 0.95–0.97 for basal area and volume, which were predicted using the metrics of height percentiles and canopy densities as independent variables. Silva et al. (2016) [26] predicted and mapped volume using LiDAR metrics in Eucalyptus plantations in tropical forests (located in São Paulo, Brazil), and found that volume ( $Adj-R^2 = 0.84$ ) was well predicted by the coefficient of variation of return height and the 99th height percentile from LiDAR. Tesfamichael and Beech (2016) [27] used height-related metrics (e.g., height percentiles, maximum height) and canopy density metrics to estimate plot-level structural attributes (i.e., mean height, maximum height, crown diameter and aboveground biomass) over a savanna ecosystem region located in the south western part of Zambia, and resulted in  $R^2$  values of 0.48–0.95. However, these studies often include height and density predictors with little physical justification for model formulation. Moreover, they usually neglected a mechanism to summarize complex canopy

characteristics into simple parameters, which can potentially be used for estimates of forest structural parameters in different forest conditions [14,28], and the standard metrics (i.e., height-based and density-based metrics) tend to be strongly inter-correlated, and depend on forest conditions, plot sizes, point cloud density and geometrical distributions of point clouds etc. [29–33], and a large subset of these metrics are linked to only a few forest stand characteristics. Thus, these metrics generally have a relatively low transferability and are limited in describing the vertical heterogeneity of forest structure [24].

Canopy vertical profiles, defined as the distributed curves about the characteristic of forest structural components as a function of height above ground, are intimately linked to the vertical distributions of forest structural elements (e.g., foliage, branches, trunks etc.), and have strong potential in enhancing the theoretical explanations of vertical forest structure [4,34,35]. Canopy vertical profiles are important descriptors of forest structure. Lefsky et al. (1999) [36] developed an approach termed “canopy volume models (CVM)” to characterize three-dimensional (3D) volumetric structure of forest canopies by quantifying the differences in the total volume and spatial organization of the tree foliage, and this approach is beneficial to distinguish specific volumetric canopy architecture. They found relatively high accuracies ( $R^2 = 0.52\text{--}0.91$ ) for estimating forest structural parameters using the metrics derived from canopy vertical profiles (i.e., canopy volume profiles (CVP) and canopy height profiles (CHP)). Lovell et al. (2003) [37] used airborne and terrestrial LiDAR data to derive foliage profiles (FP) and estimated effective leaf area index (LAI) in temperate forests located in southern Australia. They found that results compared with LAI derived from classified hemispherical photographs with agreement within 8%. Coops et al. (2007) [38] refined the CVM approach to adapt discrete return LiDAR data. In addition, a Weibull fitting approach was conducted to fit FP profiles and further obtain relevant LiDAR metrics, and finally a number of forest structural parameters (i.e., mean height, basal area) ( $R^2 = 0.65\text{--}0.85$ ) were estimated. Hilker et al. (2010) [39] assessed and compared canopy metrics derived from canopy vertical profiles using airborne and terrestrial LiDAR data. The results showed that airborne and terrestrial LiDAR were both able to accurately determine canopy height (absolute error of height was less than 2.5 m) and LAI ( $R^2 = 0.86\text{--}0.90$ ). However, most previous studies that estimate forest structural parameters using canopy metrics derived from canopy vertical profiles were conducted in temperate, tropical and boreal forests, and published studies of the subtropical forests are few.

In this study, the standard metrics and canopy metrics derived from airborne LiDAR data are used to estimate plot-level forest structural parameters (i.e., mean diameter at breast height, Lorey’s mean height, stem density, basal area, volume, and aboveground biomass) individually and in combination over a north subtropical secondary forest in southern Jiangsu Province, China. The objectives of this study are: (1) to derive two suites of canopy metrics, i.e., canopy volume (CV) metrics and Weibull-fitted (WF) metrics, using voxel-based CVM and Weibull fitting approaches separately; and (2) to assess the capability of standard metrics and canopy metrics based models and combination models for estimating forest structural parameters and to evaluate the accuracies of the models; and (3) to explore the optimal horizontal and vertical resolution of voxels for the predictive models.

## 2. Materials and Methods

An overview of the workflow for calculating plot-level forest structural parameters estimation is shown in Figure 1. Firstly, a 1-m Digital terrain model (DTM) was created by the last return points. The data was filtered to remove the above-ground returns, and then the DTM was created by calculating the average elevation from the remaining (ground) LiDAR returns within a cell. Cells that contain no points are interpolated by neighboring cells. The point cloud was then normalized against the ground surface height. Secondly, standard metrics (i.e., height-based (HB) metrics and density-based (DB) metrics) and canopy metrics (i.e., canopy volume (CV) metrics and Weibull-fitted (WF) metrics) were extracted. The suite of canopy volume (CV) metrics was derived by a voxel-based CVM approach, and another suite of WF-metrics was derived by calculating  $\alpha$  (scale) and  $\beta$  (shape) parameters of

Weibull function fitting to canopy height distribution (CHD) and FP. Thirdly, the estimation capability of standard metrics-based (SM) models, canopy metrics-based (CM) models and combination models were examined for estimating forest structural parameters separately. Finally, the accuracies of the models were assessed and validated by field measured data.

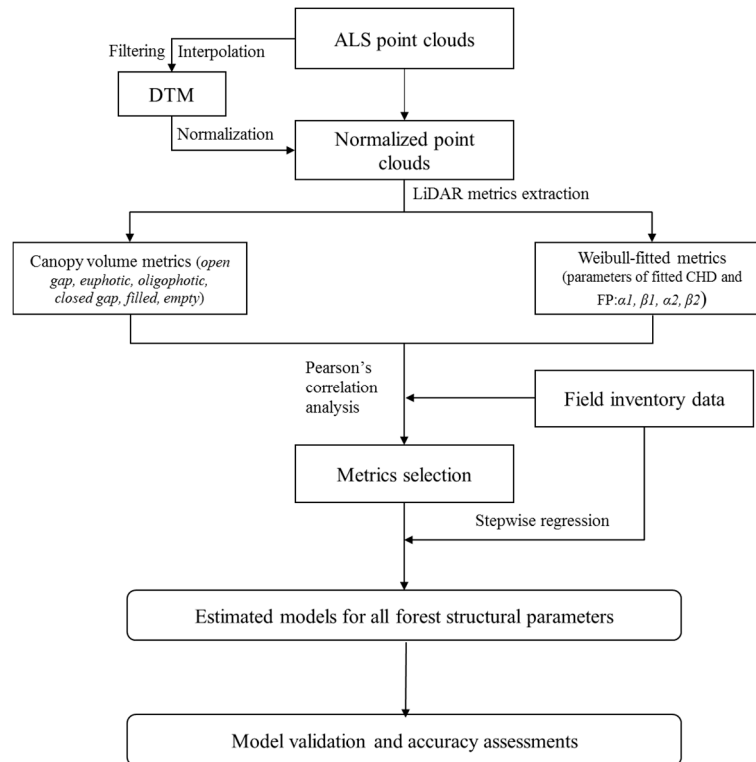


**Figure 1.** An overview of the workflow for forest structural parameters estimation. DTM: Digital Terrain Model.

### 2.1. Study Area

This study was conducted in Yushan Forest, a state-operated forest and national park located near the town of Changshu in Jiangsu Province, southeastern China ( $120^{\circ}42'9.4''E$ ,  $31^{\circ}40'4.1''N$ ). The total site area is approximately 1260 ha, which covers approximately 1140 ha of forests. Topographically, the site's mountain terrain extends from northwest to southeast and the ridge line is more than 6500 m, with the elevation range between approximately 20 and 261 m above sea level. This site is situated in the north-subtropical monsoon climatic region with an annual mean temperature of  $15.4^{\circ}C$ , and precipitation of 1047.7 mm, and annual mean relative humidity of approximately 80%. The highest monthly precipitation occurs from June to September. The soil type in Yushan is composed mainly of mountain yellow-brown earth. The forest in Yushan belongs to the north-subtropical mixed secondary forest with three main forest types: conifer-dominated, broad-leaved dominated and mixed forests. The dominant broad-leaved tree species include Oriental oak (*Quercus variabilis* Bl.), Chinese sweet gum (*Liquidambar formosana* Hance) and Sawtooth oak (*Quercus acutissima* Carruth.) of deciduous broad-leaved trees species, mixed with other evergreen broad-leaved tree species including Camphorwood (*Cinnamomum camphora* (L.) Presl.) and Chinese holly (*Ilex chinensis* Sims.). The primary coniferous forests are dominated by evergreen coniferous tree species, including Masson pine (*Pinus massoniana* Lamb.), Chinese fir (*Cunninghamia lanceolata* (Lamb.) Hook.), slash pine (*Pinus elliottii* Engelm.) and Japanese Blackbark Pine (*Pinus thunbergii* Parl.). Figure 2 shows an overview of the study site and distribution of sample plots and Figure 3 shows the field photos of three forest types.

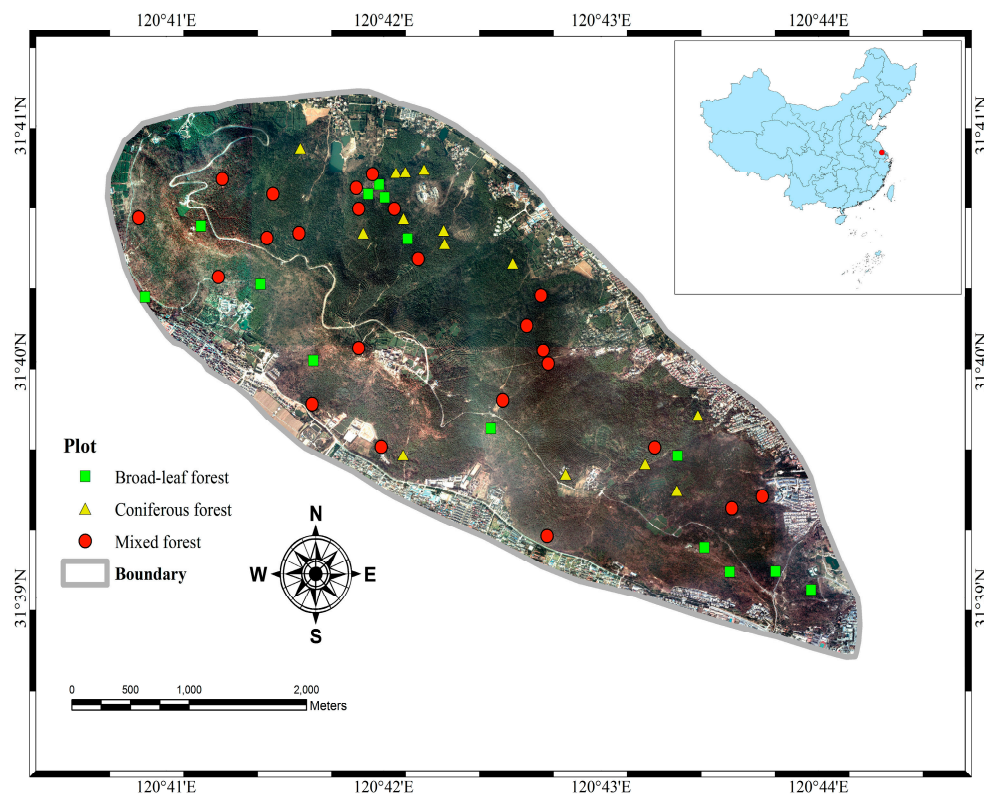


**Figure 2.** Study site and distribution of sample plots.

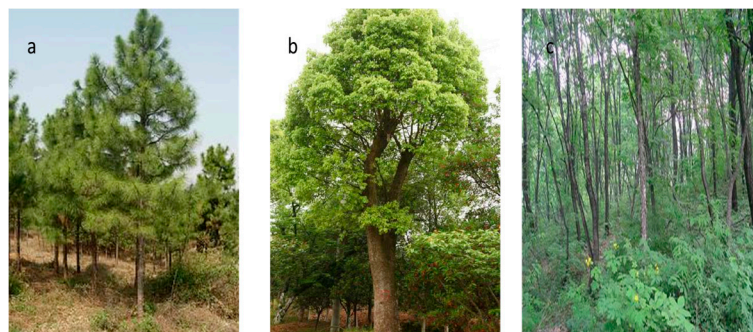


**Figure 3.** Examples of the three main forest types in study site. (a) Coniferous forest; (b) broad-leaved forest; (c) mixed forest.

## 2.2. Data Acquisition and Pre-Processing

### 2.2.1. LiDAR Data

Small footprint airborne LiDAR data were acquired on 17 August 2013 using a Riegl LMS-Q680i sensor flown at 900 m above ground level, with a flight speed of  $55 \text{ m}\cdot\text{s}^{-1}$  and a flight line side-lap of  $\geq 60\%$ . The sensor recorded returned waveforms of laser pulse with a temporal sample spacing of 1 ns (approximately 15 cm). The LiDAR system was configured to emit laser pulses in the near-infrared band (1550 nm) at a 360 kHz pulse repetition frequency and a 112 Hz scanning frequency, with a scanning angle of  $\pm 30^\circ$  from nadir and a swath of 1040 m. The dataset had an average beam footprint size of 0.45 m (nadir) in diameter. The average ground point distances of the dataset were 0.49 m (flying direction) and 0.48 m (scanning direction) in a single strip, with pulse density of approximately

5.06 pulse  $m^{-2}$ . The final extracted point clouds and associated waveforms were stored in LAS 1.3 format (American Society for Photogrammetry and Remote Sensing, Bethesda, MD, USA).

In order to obtain the relative height of trees, raw point cloud data were first filtered by removing outliers. The data were filtered to remove non-ground points using an algorithm adapted from Kraus and Pfeifer (1998) [40], which was based on a method of linear least-squares interpolation, and then the data were smoothed by the median filter (moving square windows of size  $5 \times 5$  m). After filtering the non-ground points, a 1-m Digital terrain model (DTM) was created by calculating the average elevation from the ground points within a cell (cells that contain no points were filled by interpolation using neighboring cells). Then, the point cloud was then normalized against the ground surface height and extracted for each plot. Point clouds for all plots ( $n = 51$ ) were finally extracted using the coordinates of the lower left and upper right corners.

## 2.2.2. Field Data

The field data for the study site were collected from June to August in 2012 and in August of 2013. Throughout the Yushan study region, a total of 51 square sample plots ( $30 \times 30$  m) were established, covering the forest type, dominant species compositions, age classes, and site indices, according to an historical forest resource inventory data (2012). All plots were divided into broad-leaved forest ( $n = 14$ ), coniferous forest ( $n = 14$ ), and mixed forest ( $n = 23$ ). The centers of each plot and plot corners were located using Trimble GeoXH6000 Handheld GPS (Trimble, Sunnyvale, CA, USA) units equipped with a dual frequency GNSS antenna, and corrected with high precision real-time differential signals received from the Jiangsu Continuously Operating Reference Stations (JSCORS), resulting in a submeter positional of accuracy of less than 0.5 m [41]. The plot directions and inclined angles were recorded by forest compass, and the border lengths were measured by PI tape. For all live trees with a diameter at breast height (DBH) over 5 cm, tree type, diameter, height, height to crown base, crown width in both cardinal directions, crown class, and crown transparency were measured. DBH was measured on all trees using a diameter tape. Heights of all trees were measured using a Vertex IV hypsometer (Haglöf, Långsele, Sweden). Crown widths were obtained by measuring the average of two values measured along two perpendicular directions from the location of the tree top. In addition, small trees (DBH < 5 cm) and dead wood were also tallied for total stem density, but not used in biomass calculations.

Several forest structural parameters were assessed in this study, including mean DBH, Lorey's mean height (i.e., the basal area weighted height), stem density, basal area, volume and aboveground biomass. In addition, aboveground biomass of each tree was calculated by means of the species specific allometric equations from local or nearby province [42–47] (Appendix A (Table A1)), and the tree-based calculation results were summed within each plot to determine plot-level forest aboveground biomass. Plot-level volume was similarly calculated using provincial species specific volume equations of individual trees, which were based on DBH as predictor variables. A summary of plot-level forest structural parameters data is presented in Table 1.

**Table 1.** A summary of plot-level forest structural parameters data.

Parameters	Coniferous Forest ( $n = 14$ )			Broad-Leaved Forest ( $n = 14$ )			Mixed Forest ( $n = 23$ )		
	Range	Mean	SD	Range	Mean	SD	Range	Mean	SD
DBH/cm	8.08–19.22	12.62	2.53	11.63–20.99	15.32	3.29	10.58–19.69	13.90	2.51
$h_{\text{Lorey}}$ /m	4.47–12.97	9.50	2.00	7.70–18.52	11.35	2.75	7.79–14.18	10.79	1.71
$N$ /( $ha^{-1}$ )	656–3167	1690.64	643.15	322.00–1833.00	1126.00	428.55	689.00–2344.00	1431.78	438.40
$G$ /( $m^2 \cdot ha^{-1}$ )	6.97–34.07	23.08	6.79	12.11–28.10	21.92	3.89	16.84–35.37	23.98	4.46
$V$ /( $m^3 \cdot ha^{-1}$ )	32.19–178.08	116.53	34.75	90.62–212.45	132.77	32.30	82.78–187.91	131.98	28.67
AGB/( $Mg \cdot ha^{-1}$ )	11.02–127.39	69.74	27.76	32.03–219.67	94.28	44.93	49.65–141.73	89.36	25.95

Notes: DBH: Mean diameter at breast height;  $h_{\text{Lorey}}$ : Lorey's mean height;  $N$ : Stem density;  $G$ : Basal area;  $V$ : Volume; AGB: Aboveground biomass.

### 2.3. Derived Metrics

#### 2.3.1. Canopy Volume Model Approach

A voxel-based CVM approach was applied for point cloud data to derive metrics in this study. The canopy spaces were first organized as a matrix composed of voxels ( $5 \times 5 \times 0.5 \text{ m}^3$ ), and these voxels were classified as either “filled” or “empty” volume depending on the presence or absence of LiDAR points within each voxel. “Filled” voxels were further classified as either “euphotic” zone, if they were located in the uppermost 65% of all filled voxels, or as “oligophotic” zone if they were located below the point, whereas “empty” voxels were located either below (“closed gap”) or above the canopy (“open gap”) [38]. Open gap, euphotic, oligophotic and closed gap were determined as four canopy structure classes, with units defined as the volume of each class per unit area. All volume elements (*Open gap*, *Oligophotic*, *Euphotic*, *Closed gap*, *Filled*, *Empty*) were derived as canopy volume (CV) metrics using the CVM method and canopy volume profile (CVP) was visualized. Figure 4 shows the illustration of voxel-based CVM approach. Point clouds of a plot ( $30 \times 30 \text{ m}^2$ ) were voxelized, and divided into 36 vertical columns of voxels, and each column was further stratified with four canopy structure classes. All columns of a plot were expanded in a panel and the canopy volume distribution (CVD) was presented (Figure 4c). Finally, the volume percentages of canopy structure classes of each height interval (0.5 m) were calculated, resulting in CVP (Figure 4d).

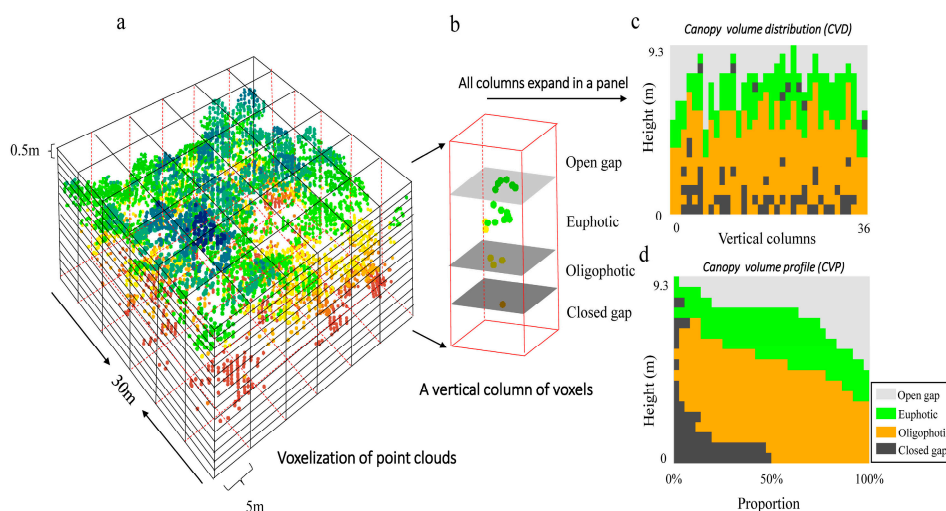


**Figure 4.** The illustration of voxel-based canopy volume model. (a) A plot ( $30 \times 30 \text{ m}^2$ ) was stratified with voxelization and height bin is 0.5 m; (b) a voxel column was stratified in four structure classes (open gap, euphotic, oligophotic, closed gap) with canopy volume model approach; (c) canopy volume distribution, which shows the distribution of canopy structure classes after all columns were expanded in a panel; (d) the canopy volume profile, which was transformed from the canopy volume distribution diagram, shows the volume percentage of each class of total volume in each height interval.

Notably, an appropriate voxel volume size for CVM in this study was been considered because various voxel sizes likely change the distributions and proportions of canopy structure classes. Thus, this study also investigated the influence of various voxel sizes on the accuracies of the models. Given the average beam footprint size of 0.45 m, average ground point distances of 0.49 m (flying direction) and 0.48 m (scanning direction) and pulse density of approximately  $5.06 \text{ pulse} \cdot \text{m}^{-2}$ , horizontal resolutions of 1 m to 10 m were chosen (which were multiples of the footprint size and average ground point distances). Vertical resolutions of 0.5 m and 1 m were chosen to correspond to roughly three and six sampling intervals of the returned waveform. A sensitivity analysis was performed using CV-metrics (i.e., *Open gap*, *Oligophotic*, *Euphotic*, *Closed gap*, *Filled*, *Empty*).

### 2.3.2. Weibull Fitting Approach

Canopy height distributions (CHD), which describe vertical distributions of foliage elements and non-photosynthetic tissues within canopy spaces, were used to measure the distribution of laser returns within the 0.3-m bins (i.e., a  $30 \times 30 \times 0.3 \text{ m}^3$  rectangular section) from the ground to canopy top [48,49]. In this study, a two-parameter Weibull density function (PDF) was used to describe CHD on each plot. As a Weibull model is highly adaptive, ranging from an inversed J-shape to unimodal skewed and unimodal symmetrical curve, the Weibull model has flexibility in characterizing distributions of a range of forest attributes [50,51]. The two parameters, i.e., Weibull scale ( $\alpha_1$ ) and Weibull shape ( $\beta_1$ ), were derived by the maximum likelihood estimation method. Weibull scale determines the basic shape of the distribution density curve and Weibull shape controls the breadth of the distribution [52]. Foliage profile (FP) can delineate the vertical distribution of canopy phytoelement (e.g., leaf, stem, twig, etc.) density above the ground within a forest stand [37]. FP is defined as the total one-sided leaf area that is involved in photosynthesis per unit canopy volume at canopy height  $z$ , and describes changes in the leaf area distribution with increasing height [53]. FP is highly related to leaf area index (LAI), which was demonstrated in previous studies [35,54], and the relationship between FP and LAI is:

$$L(z) = \int_{z_1}^{z_2} FP(z) dz, \quad (1)$$

where  $L(z)$  is the cumulative leaf area index (LAI<sub>c</sub>) from the ground to a given height  $z$ ;  $FP(z)$  represents the foliage area volume density at height  $z$  (is the vertical foliage profile in a thin layer or “slice” through a canopy as a function of height  $z$ );  $z_1$  and  $z_2$  are different canopy height. A height interval or each vertical “slice” was 0.3 m. Meanwhile, we assumed that foliage elements in a thin “slice” were very small so that occlusion can be neglected, and leaves presented Poisson random distribution. Because airborne LiDAR is incapable of resolving foliage angle distribution, clumping and non-foliage elements, the foliage profiles derived from airborne LiDAR are referred to here as “apparent” foliage profiles and effective LAI [37]. In this study, LAI can be indirectly determined from LiDAR by estimating the derived gap probability in the canopy [37,38], and the gap probability be estimated as the total number of laser hits up to a height  $z$  relative to the total number of LiDAR shots as follows:

$$L(z) = -\ln(P_{gap}(z)) = -\ln\left(1 - \frac{(\#z_j | z_j > z)}{N}\right), \quad (2)$$

where  $P_{gap}(z)$  is a gap probability measurement at height  $z$ ,  $\#z$  is the number of hits down to a height  $z$  above the ground, and  $N$  is the total number of shots emitted up to the sky. Previous studies have showed that Weibull distribution function can also delineate vertical foliage profiles distributions [37,55]. In this study, the Weibull fitted scale parameter ( $\alpha_2$ ) and shape parameter ( $\beta_2$ ) were derived from the apparent FP by linking Weibull cumulative function to cumulative projected foliage area index [37,38]:

$$L(z) = 1 - \left(e^{-\left(\frac{1-z/H_{\max}}{\alpha_2}\right)^{\beta_2}}\right), \quad (3)$$

where  $\alpha_2$  and  $\beta_2$  are fitted parameters,  $z$  is the height, and  $H$  is the maximum height in a plot.

Moreover, another suite of standard metrics were calculated, including height-based (HD) metrics ( $h_{25}$ ,  $h_{50}$ ,  $h_{75}$ ,  $h_{95}$ ,  $h_{\text{mean}}$ ,  $h_{\text{cv}}$ ,  $h_{\text{skewness}}$  and  $h_{\text{kurtosis}}$ ) and density-based (DB) metrics ( $d_1$ ,  $d_3$ ,  $d_5$ ,  $d_7$ ,  $d_9$ ,  $CC_{2m}$ ). A summary of these metrics with corresponding descriptions is shown in Table 2.

**Table 2.** The description of LiDAR canopy metrics.

LiDAR Metrics		Description
Standard metrics		
Height-based	Percentile heights ( $h_{25}$ , $h_{50}$ , $h_{75}$ and $h_{95}$ )	The percentiles of the canopy height distributions (25th, 50th, 75th and 95th) of first returns.
	Mean height ( $h_{\text{mean}}$ )	Mean height above ground of all first returns.
	Coefficient of variation of heights ( $h_{\text{cv}}$ )	Coefficient of variation of heights of all first returns.
	Skewness and Kurtosis of heights (i.e., $h_{\text{skewness}}$ and $h_{\text{kurtosis}}$ )	The skewness and kurtosis of the heights of all points.
Density-based	Canopy return density ( $d_1$ , $d_3$ , $d_5$ , $d_7$ and $d_9$ )	The proportion of points above the quantiles (10th, 30th, 50th, 70th and 80th) to total number of points.
	Canopy cover above 2 m ( $CC_{2m}$ )	Percentages of first returns above 2 m.
Canopy metrics		
Canopy volume	Filled and Empty zones of CVM (i.e., <i>Filled</i> and <i>Empty</i> )	The voxels contained point clouds and voxels contained no point clouds within canopy spaces.
	Open and Closed gap zones of CVM (i.e., <i>Open gap (OG)</i> and <i>Closed gap (CG)</i> )	The empty voxels located above and below the canopy respectively.
	Euphotic and Oligophotic zones of CVM (i.e., <i>Euphotic (Eu)</i> and <i>Oligophotic (Oligo)</i> )	The voxels located within an uppermost percentile (65%) of all filled grid cells of that column, and voxels located below the point in the profile
Weibull-fitted	$\alpha_1$ and $\beta_1$ parameter of Weibull distribution	The scale parameter $\alpha$ and shape parameter $\beta$ of the Weibull density distribution fitted to CHD.
	$\alpha_2$ and $\beta_2$ parameter of Weibull distribution	The scale parameter $\alpha$ and shape parameter $\beta$ of the Weibull density distribution fitted to FP.

#### 2.4. Metrics Selection and Statistical Analysis

All of the LiDAR metrics in Table 2 were used to analyze pair-wise relationships among different forest structural parameters (DBH, Lorey's mean height, stem density, basal area, volume and AGB) by Pearson's correlations ( $r$ ). Then the metrics with low correlations ( $r < 0.2$ ) were excluded and candidate metrics were used in the regression analysis. In the multiple regression analysis, all of the dependent variables and independent variables were transformed using the natural logarithm to improve linearity and corrected for bias using a bias correction factor (BCF) [56]. Some studies have applied log transformations to both dependent variables and independent variables for estimations of forest parameters [57,58]. Multiple regression models including forest type-specific (coniferous forest, broad-leaved forest, and mixed forest) models and general models of all plots were then established. Both stepwise variable selection and the maximum coefficient of determination ( $R^2$ ) improvement variable selection techniques were applied to select the metrics to be included in the models [59]. Independent variables were left in the model using an F-test with a  $p < 0.05$  significance level. The standard least-squares method was used [60].

To ensure that the independent variables were not highly correlated, multicollinearity was evaluated using Principal Component Analysis (PCA) based on the correlation matrix. Models with condition number ( $k$ ) lower than 30 were accepted to ensure that there was no serious multicollinearity in the selected models [57]. The best fitting models were then selected based on the lowest Akaike information criterion value [61]. The accuracies of predictive models were evaluated using adjusted coefficient of determination ( $Adj-R^2$ ), Root-Mean-Square Error ( $RMSE$ ), which has been transformed back to original scale, and relative  $RMSE$  ( $rRMSE$ ), which are defined as the percentage of the ratio of  $RMSE$  and the observed mean values. In this study, dummy variables (or class variables) were added to the selected models as the dependent variables to assess whether these models differ between

forest types [62]. Once the best models were chosen, leave-one-out cross-validation was performed to evaluate the predictive accuracies of the models [63].

$$Adj - R^2 = 1 - \frac{n-1}{n-p-1}(1 - R^2) \quad (4)$$

$$RMSE = \sqrt{\frac{1}{n} \sum_{i=1}^n (x_i - \hat{x}_i)^2} \quad (5)$$

$$rRMSE = \frac{RMSE}{\bar{x}} \times 100\%, \quad (6)$$

where  $x_i$  is the observed value for plot  $i$ ,  $\bar{x}$  is the observed mean value for plot  $i$ ,  $\hat{x}_i$  is the estimated value for plot  $i$ ,  $n$  is the number of plots  $i$ , and  $p$  is the number of variables.

### 3. Results

#### 3.1. Profile Analysis

The plots of each forest type were stratified into three groups (low, medium, and high), according to the Lorey's mean height from low to high. In each group, three plots were selected, and a total of nine typical plots were selected. For the typical plots, CVD, CVP and FP were extracted, as shown in Figures 5–7. In addition, Figure 8 shows the mean LAI<sub>c</sub> for plots in different forest types and mean CVD.

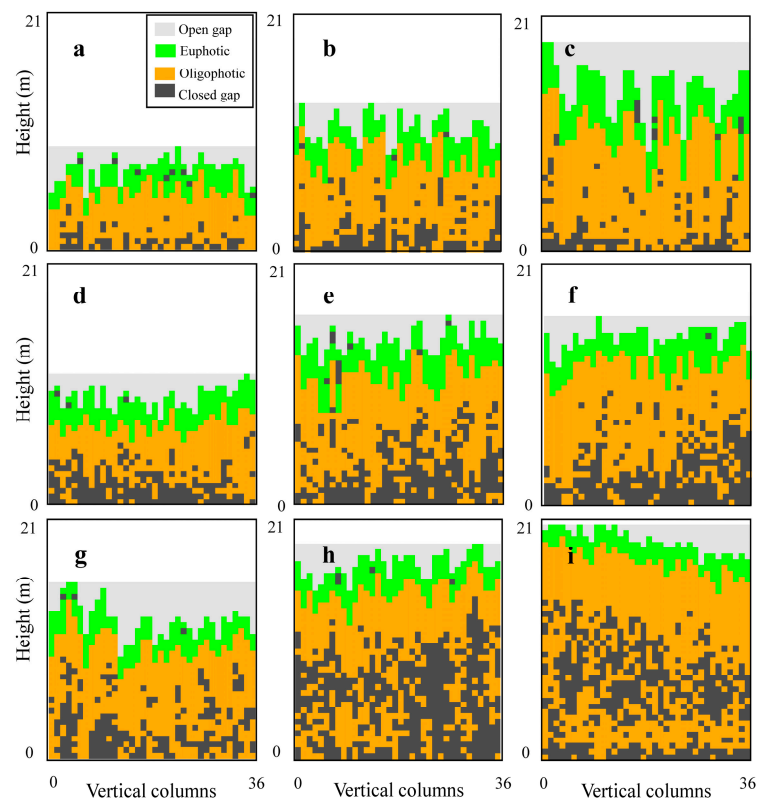


**Figure 5.** Canopy volume distributions for the plots in different forest types. (a–c) Three typical plots of coniferous forest; (d–f) three typical plots of mixed forest; (g–i) three typical plots of broad-leaved forest.

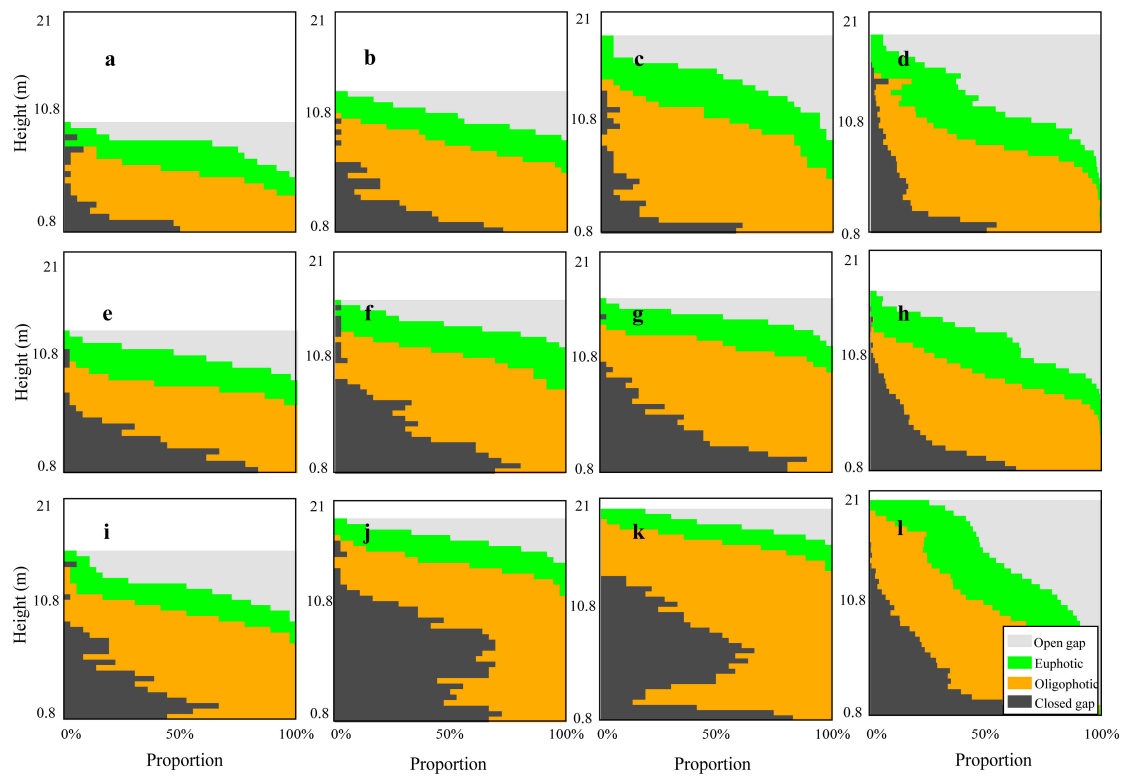


**Figure 6.** Canopy volume profiles for the plots in different forest types. (a–c) Three typical plots of coniferous forest; (e–g) three typical plots of mixed forest; (i–k) three typical plots of broad-leaved forest; (d,h,l) the mean canopy volume profiles in each forest.

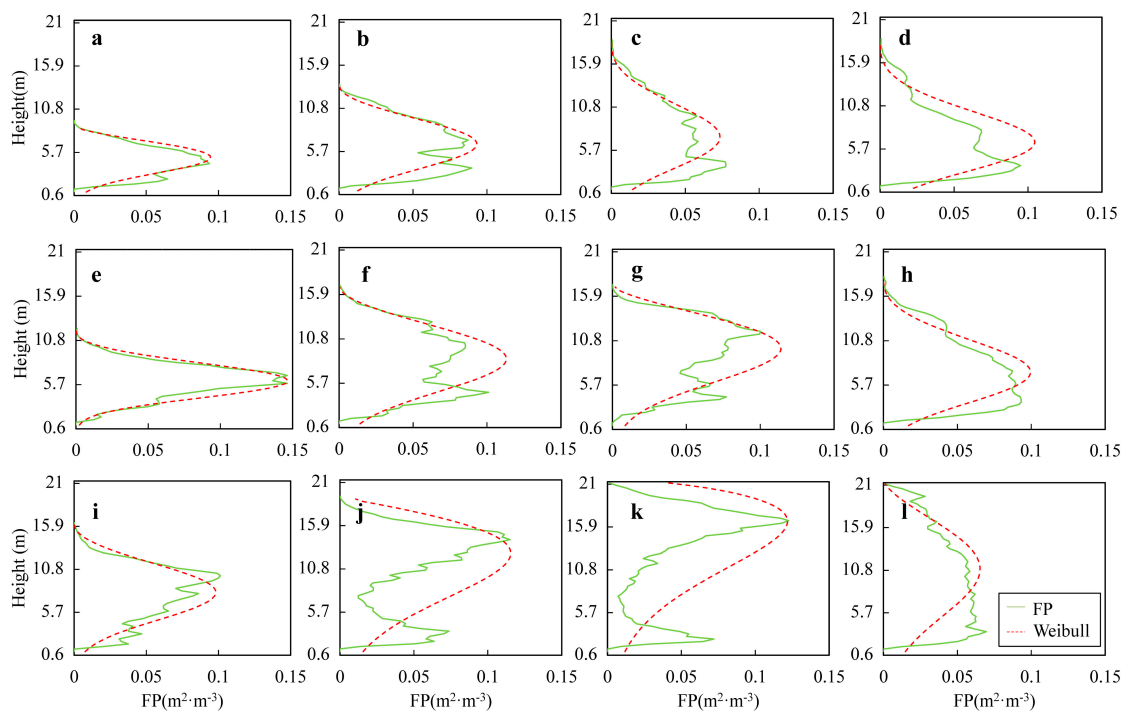


**Figure 7.** Foliage profiles for the plots in different forest types. (a–c) Three typical plots of coniferous forest; (e–g) three typical plots of mixed forest; (i–k) three typical plots of broad-leaved forest; (d,h,l) the mean foliage profiles in each forest type.

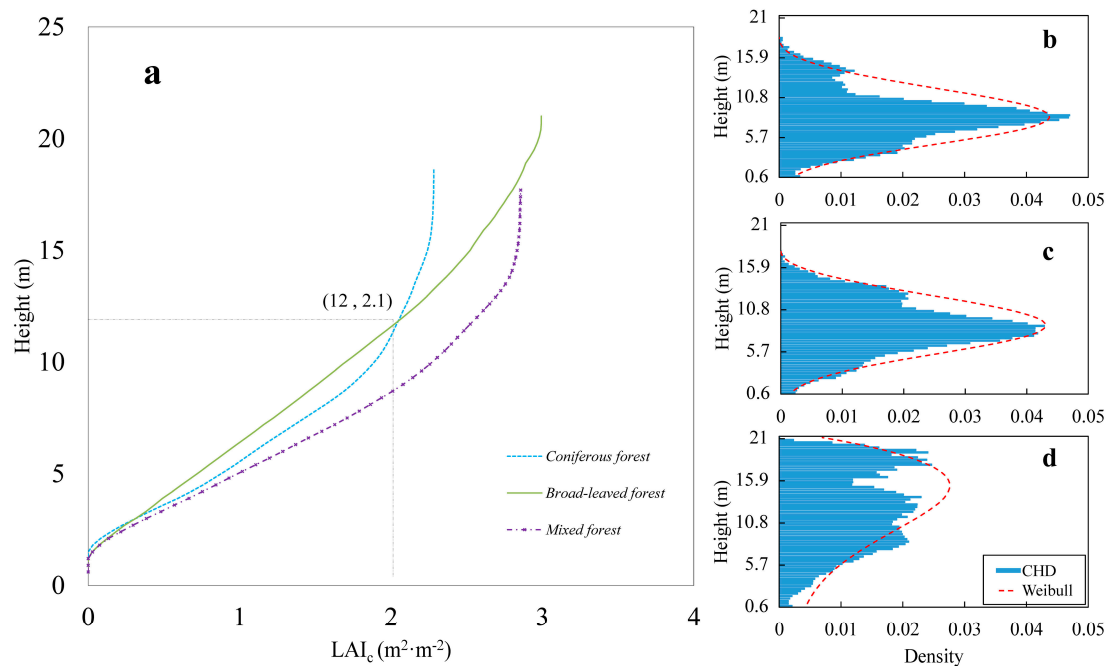


**Figure 8.** The mean cumulative leaf area index profiles for plots in different forest types (a) and mean canopy height distribution: (b) coniferous forest; (c) mixed forest; (d) broad-leaved forest.

Figure 5 shows the spatial arrangements of four canopy structure classes for coniferous, broad-leaved, and mixed forest plots. Generally, Oligophotic zones were larger than euphotic zone in filled volume; coniferous forests had the largest open gap zone and the smallest closed gap zone, whereas broad-leaved forests plots had a larger and wider spread of closed gap zone than mixed forest. Similarly, the percentage of closed gap volume was larger in broad-leaved forests than in mixed forests, and the lowest percentage of closed gap volume was in coniferous forests (Figure 6). The mean CVPs (Figure 6d,h,l) show that the percentages of open gap volume were the highest in coniferous forests, and the differences were not significant between the percentages of open gap volume in broad-leaved forests and mixed forests. The percentages of filled volume in coniferous and mixed forests were significantly higher than in broad-leaved forest, and the differences for the percentage of filled volume between coniferous and mixed forest were not significant.

Weibull models were fitted to canopy foliage distribution and matched the shape of foliage profile relatively well (Figure 7). In general, the FP profiles first exhibited a strong increasing trend, followed by a decreasing trend. Particularly, the peaks of FP in coniferous and mixed forests occurred in the lower or middle portions of the canopies whereas the peaks of broad-leaved forests were distributed more toward middle and upper portions of the canopies. Comparing with the mean foliage profiles and Weibull curves of three forest types, the curve showing the spatial distribution of FP values was smoother in broad-leaved forests than those of coniferous or mixed forests. The Weibull shapes of mixed forest canopy were slightly steeper than those of coniferous forest stands, indicating a wider spread of foliage within the canopy (Figure 7d,h,l). This same trend can be seen in the mean CHDs (Figure 8b–d).

The mean LAI<sub>c</sub> values below the threshold of 12 m (approximately middle canopy) were relatively high for mixed forests, followed by coniferous forests and broad-leaved forests (Figure 8a). Above the tree height of 12 m, the increasing slope of the mean LAI<sub>c</sub> of the broad-leaved forests with increasing tree height was higher than that of coniferous forests, and maintained a relative high increasing trend, whereas the increasing trend of coniferous forests and mixed forests gradually tended to saturate. As a result, the mean LAI<sub>c</sub> value of broad-leaved forests was eventually higher than that of mixed forests, and lowest for coniferous forests.

### 3.2. Accuracy Assessments

The selected metrics and accuracy assessment results of all the multi-regression models (i.e., SM models, CM models, and combination models) are shown in Tables A1–A3 and Table 3 summarizes their accuracies. All of the forest structural parameters were generally well estimated ( $Adj-R^2 = 0.39–0.88$ ,  $rRMSE = 5.13–29.86\%$ ). Overall, Lorey's mean height ( $Adj-R^2 = 0.61–0.88$ ,  $rRMSE = 5.13–12.79\%$ ) and AGB ( $Adj-R^2 = 0.54–0.81$ ,  $rRMSE = 12.19–28.42\%$ ) was predicted most accurately. For volume, DBH and basal area, the  $R^2$  values were slightly lower and ranged from 0.42 to 0.78, 0.48 to 0.74 and 0.41 to 0.69, respectively. The lowest accuracy was found for stem density ( $Adj-R^2 = 0.39–0.64$ ,  $rRMSE = 18.68–29.86\%$ ). In comparison, most of forest structural parameters in type-specific models ( $Adj-R^2 = 0.44–0.88$ ,  $rRMSE = 5.13–28.42\%$ ) had higher accuracies than in general models ( $Adj-R^2 = 0.39–0.77$ ,  $rRMSE = 8.54–29.86\%$ ), indicating that the accuracies of forest type-specific models were generally improved rather than general models. Furthermore, the fitted models of the forest structural parameters were relatively more accurate for coniferous forests ( $Adj-R^2 = 0.54–0.81$ ,  $rRMSE = 8.59–26.55\%$ ) than broad-leaved forests ( $Adj-R^2 = 0.50–0.88$ ,  $rRMSE = 6.39–28.42\%$ ) and mixed forests ( $R^2 = 0.44–0.84$ ,  $rRMSE = 5.13–29.52\%$ ). Compared with canopy metrics based models ( $Adj-R^2 = 0.39–0.83$ ,  $rRMSE = 6.94–29.26\%$ ), standard metrics based models had a relatively higher performance ( $Adj-R^2 = 0.42–0.84$ ,  $rRMSE = 5.60–29.86\%$ ) and the combination models performed best ( $Adj-R^2 = 0.45–0.88$ ,  $rRMSE = 5.13–28.96\%$ ), indicating the inclusion of canopy metrics potentially improved the estimation performances of structural parameters.

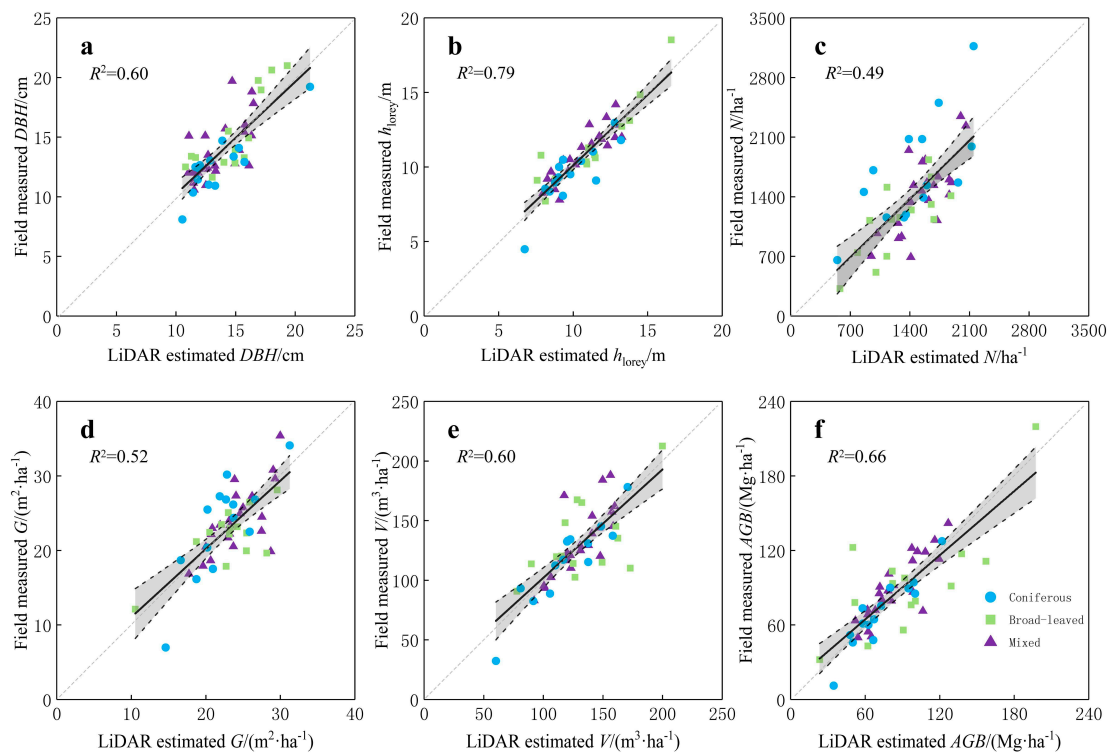
For all of the general SM models, the standard metrics that were regressed against for fitting models included most of the standard metrics, indicating those had a relatively strong correlation with forest structural parameters. Overall,  $h_{95}$  (selected by four out of six models),  $d_7$  (selected by four out of six models),  $d_3$ ,  $h_{CV}$  and  $d_9$  (each of them was selected by three out of six models) were the most frequently selected, indicating these metrics are more sensitive and representative to the forest structural parameters. For general CM models, all of CV metrics and WF metrics were selected for estimating forest structural parameters. Within CV metrics, the statistic of *Oligophotic* (all selected by six models), *Empty* (selected by four out of six models) and *Open* (selected by four out of six models) were sensitive to forest structural parameters and these metrics were selected both in the general models and forest type-specific models, suggesting that the three metrics have a strong ability to explain variations. Within WF metrics,  $\alpha_1$  was relatively sensitive to structural parameters (selected two out of six models). In six general combination models, most of standard metrics (nine out of 14) and canopy metrics (four out of total 10) were used in combination for parameter estimations. The metrics of *Oligophotic*, *Empty*,  $h_{95}$  remained sensitive to structural parameters (selected by 2–4 out of six general combo models). Moreover,  $h_{75}$ ,  $d_1$  and  $\beta_1$  (selected by 2–3 out of 6) became more sensitive for DBH, Lorey's mean height, and stem density in combination models than SM models.

Figure 9 shows the LiDAR estimated versus the field measured forest structural parameters as well as the results for cross-validation in all plots models based on standard metrics and canopy metrics. As indicated, Lorey's mean height and AGB models were fitted best and resulted in  $R^2$  values of 0.79 and 0.66, followed by DBH ( $R^2 = 0.60$ ), volume ( $R^2 = 0.60$ ) and basal area ( $R^2 = 0.52$ ), whereas the accuracy of stem density model was the lowest ( $R^2 = 0.49$ ). For Lorey's mean height, AGB, DBH, and volume estimations, their relationships were close to the 1:1 line whereas basal area and stem density had a relationship that deviated from the 1:1 line, with a slightly larger deviation in broad-leaved forests.

**Table 3.** A summary of selected metrics and accuracy assessment results of predictive models.

Forest Types	Parameters	SM Models				CM Models				Combination Models			
		Standard Metrics	Adj-R <sup>2</sup>	RMSE	rRMSE %	Canopy Metrics	Adj-R <sup>2</sup>	RMSE	rRMSE %	All Metrics	Adj-R <sup>2</sup>	RMSE	rRMSE %
All plots	DBH/cm	$h_{95}, d_1, d_7$	0.60 ***	1.72	12.33	OG, Oligo, Empty, $\beta_2$	0.50 ***	1.86	13.31	$h_{cv}, h_{75}, d_1, Oligo$	0.61 ***	1.67	11.97
	$h_{Lorey}/m$	$h_{cv}, h_{95}, d_7, d_9$	0.75 ***	0.97	9.15	Oligo, Filled, Empty, $\alpha_1$	0.61 ***	1.18	11.13	$h_{50}, d_1, Empty, \beta_1$	0.77 ***	0.90	8.54
	$N/(ha^{-1})$	$h_{cv}, d_1, d_7, d_9$	0.42 ***	423.75	29.86	OG, Eu, Oligo, $\beta_1$	0.39 ***	415.17	29.26	$d_1, Oligo, \alpha_1, \beta_1$	0.45 ***	410.02	28.90
	$G/(m^2 \cdot ha^{-1})$	$h_{95}, d_3, d_7$	0.44 ***	3.99	17.23	Oligo, Empty, $\alpha_2$	0.41 ***	3.67	15.82	$h_{kurtosis}, h_{25}, h_{95}, Empty$	0.50 ***	3.47	14.96
	$V/(m^3 \cdot ha^{-1})$	$h_{cv}, h_{25}, h_{50}, d_3$	0.46 ***	22.34	17.46	OG, Eu, Oligo, $\alpha_1$	0.42 ***	22.36	17.48	$h_{75}, Oligo, Empty, \beta_1$	0.58 ***	21.07	16.47
	AGB/(Mg·ha <sup>-1</sup> )	$h_{kurtosis}, h_{95}, d_3, d_9$	0.64 ***	19.17	22.47	OG, Oligo, CG, Empty	0.54 ***	19.84	23.25	$h_{95}, d_3, CC_{2m}, Oligo$	0.66 ***	18.25	21.39
Coniferous forest	DBH/cm	$h_{95}, d_1, d_7$	0.67 **	1.20	9.50	OG, Oligo, Empty, $\beta_2$	0.54	1.40	11.09	$h_{cv}, h_{75}, d_1, Oligo$	0.74 **	1.08	8.59
	$h_{Lorey}/m$	$h_{cv}, h_{95}, d_7, d_9$	0.66	1.09	11.47	Oligo, Filled, Empty, $\alpha_1$	0.64	1.21	12.79	$h_{50}, d_1, Empty, \beta_1$	0.77 **	0.99	10.43
	$N/(ha^{-1})$	$h_{cv}, d_1, d_7, d_9$	0.60	315.78	18.68	OG, Eu, Oligo, $\beta_1$	0.58	431.65	25.53	$d_1, Oligo, \alpha_1, \beta_1$	0.64	339.29	20.07
	$G/(m^2 \cdot ha^{-1})$	$h_{95}, d_3, d_7$	0.62 **	4.53	19.63	Oligo, Empty, $\alpha_2$	0.55	4.73	20.48	$h_{kurtosis}, h_{25}, h_{95}, Empty$	0.69 **	4.23	18.32
	$V/(m^3 \cdot ha^{-1})$	$h_{cv}, h_{25}, h_{50}, d_3$	0.69 **	22.40	19.22	OG, Eu, Oligo, $\alpha_1$	0.72 **	18.32	15.72	$h_{75}, Oligo, Empty, \beta_1$	0.78 **	18.21	15.63
	AGB/(Mg·ha <sup>-1</sup> )	$h_{kurtosis}, h_{95}, d_3, d_9$	0.72 **	16.86	24.17	OG, Oligo, CG, Empty	0.74 **	18.51	26.55	$h_{95}, d_3, CC_{2m}, Oligo$	0.81 **	14.53	20.83
Broad-leaved forest	DBH/cm	$h_{95}, d_1, d_7$	0.61 **	1.70	11.12	OG, Oligo, Empty, $\beta_2$	0.51	1.81	11.79	$h_{cv}, h_{75}, d_1, Oligo$	0.68	1.54	10.06
	$h_{Lorey}/m$	$h_{cv}, h_{95}, d_7, d_9$	0.84 ***	0.78	6.91	Oligo, Filled, Empty, $\alpha_1$	0.83 ***	0.88	7.72	$h_{50}, d_1, Empty, \beta_1$	0.88 ***	0.72	6.39
	$N/(ha^{-1})$	$h_{cv}, d_1, d_7, d_9$	0.60	298.99	26.55	OG, Eu, Oligo, $\beta_1$	0.52	299.82	26.63	$d_1, Oligo, \alpha_1, \beta_1$	0.62	273.49	24.29
	$G/(m^2 \cdot ha^{-1})$	$h_{95}, d_3, d_7$	0.54	2.62	11.96	Oligo, Empty, $\alpha_2$	0.50	2.74	12.48	$h_{kurtosis}, h_{25}, h_{95}, Empty$	0.63	2.49	11.34
	$V/(m^3 \cdot ha^{-1})$	$h_{cv}, h_{25}, h_{50}, d_3$	0.56	19.49	14.68	OG, Eu, Oligo, $\alpha_1$	0.58	18.97	14.28	$h_{75}, Oligo, Empty, \beta_1$	0.67	16.65	12.54
	AGB/(Mg·ha <sup>-1</sup> )	$h_{kurtosis}, h_{95}, d_3, d_9$	0.57	26.80	28.42	OG, Oligo, CG, Empty	0.60	26.45	28.05	$h_{95}, d_3, CC_{2m}, Oligo$	0.66	26.67	28.29
Mixed forest	DBH/cm	$h_{95}, d_1, d_7$	0.48 **	1.66	11.94	OG, Oligo, Empty, $\beta_2$	0.48	1.78	12.79	$h_{cv}, h_{75}, d_1, Oligo$	0.55 **	1.58	11.34
	$h_{Lorey}/m$	$h_{cv}, h_{95}, d_7, d_9$	0.81 ***	0.60	5.60	Oligo, Filled, Empty, $\alpha_1$	0.75 ***	0.75	6.94	$h_{50}, d_1, Empty, \beta_1$	0.84 ***	0.55	5.13
	$N/(ha^{-1})$	$h_{cv}, d_1, d_7, d_9$	0.48 **	336.73	28.52	OG, Eu, Oligo, $\beta_1$	0.44	324.73	22.68	$d_1, Oligo, \alpha_1, \beta_1$	0.50 ***	319.05	22.28
	$G/(m^2 \cdot ha^{-1})$	$h_{95}, d_3, d_7$	0.45 **	3.08	12.86	Oligo, Empty, $\alpha_2$	0.45 ***	3.12	13.01	$h_{kurtosis}, h_{25}, h_{95}, Empty$	0.56 **	2.77	11.56
	$V/(m^3 \cdot ha^{-1})$	$h_{cv}, h_{25}, h_{50}, d_3$	0.60 ***	16.76	12.70	OG, Eu, Oligo, $\alpha_1$	0.65 ***	16.31	12.36	$h_{75}, Oligo, Empty, \beta_1$	0.71 ***	15.87	12.02
	AGB/(Mg·ha <sup>-1</sup> )	$h_{kurtosis}, h_{95}, d_3, d_9$	0.64 ***	13.20	14.77	OG, Oligo, CG, Empty	0.71 ***	13.00	14.55	$h_{95}, d_3, CC_{2m}, Oligo$	0.79 ***	10.89	12.19

Notes: Level of significance: NS = not significant (>0.05); \*\* <0.01; \*\*\* <0.001; DBH: mean diameter at breast height;  $h_{Lorey}$ : Lorey's mean height; N: Stem density; G: Basal area; V: Volume; AGB: Aboveground biomass. OG: Open gap; Oligo: Oligophotic; Eu: Euphotic; CG: Closed gap.



**Figure 9.** Scatter plots of field-measured and LiDAR estimated mean diameter at breast height (a), Lorey's mean height (b), stem density (c), basal area (d), volume (e) and aboveground biomass (f) for cross-validation in combination models.

### 3.3. The Selection of Voxel Sizes

In this study, a sensitivity analysis was performed using different voxel sizes to derive CV metrics based on CVM approach and to quantify their influence on the results. As shown in Figure 10, a quantitative comparison of estimation accuracy for four main forest structural parameters (i.e., DBH, Lorey's mean height, stem density, and basal area) was performed. In general, the  $R^2$  values of the models showed a trend of first increasing and then decreasing when horizontal resolutions of voxels were varied from 1 m to 10 m (Figure 10a,b), and the voxels in horizontal resolution of 5 m had the best performance. Figure 10a was subtracted from Figure 10b to calculate the result of Figure 10c, which demonstrated the difference of  $rRMSE$  values of forest structural parameters for various vertical resolutions (0.5 m and 1 m). The values presented were mostly positive, except for some of the differences were negative (e.g.,  $G$  at 3 m horizontal resolution) (Figure 10c). In particular, DBH and stem density models had all positive values across 1 m to 10 m of horizontal resolutions, indicating the two parameters were strongly influenced by the vertical resolution of the voxels. As a result, the suitable voxel size in this study was  $5 \times 5 \times 0.5 \text{ m}^3$ .

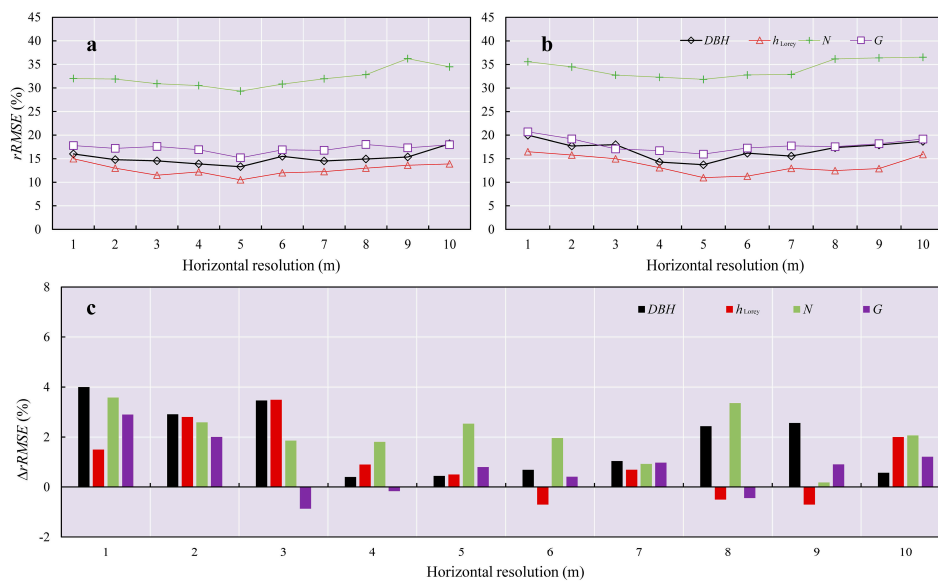


**Figure 10.** Comparison of the forest structural parameters estimation accuracies for different voxel sizes. (a) The vertical resolution of voxel sizes is 0.5 m and the horizontal resolutions range from 1 m to 10 m; (b) the vertical resolution of voxel sizes is 1 m and the horizontal resolution range from 1 m to 10 m; (c) comparison of the difference of  $rRMSE$  values ( $\Delta rRMSE$ ) of model accuracies between vertical resolution 0.5 m and vertical resolution 1 m.  $DBH$ : mean diameter at breast height;  $h_{\text{Lorey}}$ : Lorey's mean height;  $N$ : Stem density;  $G$ : Basal area.

## 4. Discussion

### 4.1. Canopy Vertical Profiles

Canopy is an important constituent of forest structure [64], and canopy structure is critical for estimation of forest structural parameters [65]. Canopy vertical profile is one of the means to quantify and analyze complex forest canopy structure and further characterize the potential heterogeneity of forest spatial structure [66]. A wide range of forest structural parameters can be directly quantified from canopy vertical profiles such as canopy height and canopy vertical distribution [67]. Also, a set of forest structural parameters (aboveground biomass, basal area, volume, LAI, canopy cover, etc.) can be predicted by establishing empirical models from LiDAR data [68]. In this study, a voxel-based CVM and Weibull fitting approach were conducted to extract two key suites of metrics for estimating forest structural parameters and derive correlative canopy vertical profiles including CVD, CVP, CHD, FP, and  $LAI_c$ . As mentioned above, the CVM approach provides a broad classification approach to categorize the canopy into photosynthetically active and less active zones [39]. Therefore, it can better reflect the spatial heterogeneity of forest structure, which is caused by the difference of light environment in the canopy. Furthermore, the CVP explicitly presented variation in the spatial arrangement of elements (i.e., open gap, euphotic, oligophotic, closed gap) within the vertical forest canopy [38]. As shown in Figures 5 and 6, the broad-leaved forests had the largest closed gap volume and the smallest open gap volume when compared to coniferous forests and mixed forests. The explanations of these phenomena need to take into account the canopy geometry and tree architecture [36]. At our research site, coniferous forests are dominated by Masson pine and slash pine; these species usually consist of a regular and conical crown, demonstrating a heavily thinned upper canopy and a dense sub-canopy (Figure 3). Furthermore, more open upper canopies in coniferous stands allow more light to pass through to the lower canopy strata [69,70], so a shrubby understory may incrementally emerge, resulting in the most open gap and the lowest closed gap zones in coniferous forests. Conversely and notably, broadleaves with elliptical or spherical crown are very tall and have positively skewed canopies with a lower canopy transparency in this study area, as

indicated by the large decrease in open gap zones. Additionally, the closed canopy volume generally increased with decreasing stand density [55], hence the broad-leaved forests with a lower stem density ( $1126.00 \text{ ha}^{-1}$ ) also had a more closed canopy gap. Although with a much more shrubby understory, mixed conifer–broadleaf forests generally encompass median height broadleaved trees [65] with a high stem density ( $1431.78 \text{ ha}^{-1}$ ) and canopy transparency, resulting in a higher amount of closed gap volume than coniferous forests and a slightly higher amount of open gap volume. On the other hand, as Yushan forest is in secondary succession, the forest canopy surface became more uneven, and the competitions among shade-intolerant species (e.g., Masson pine, Chinese sweet gum) were accelerated and further inhibited the establishment and growth of these species [71,72]. As a result, in late-successional stage, the shade-tolerant species (e.g., Oriental oak, camphorwood and Chinese holly) eventually dominated the canopy [69,72,73] and coexisted with other species. This process could cause the transmittance of light through the canopy to decline [74], which may result in an increase the spatial heterogeneity of the light environment [75,76] and a further enhancement of more microsite light availability in lower canopies [70,76–79]. Thus, for each forest type, the oligophotic zone, which represented a larger proportion of the total filled volume compared to the euphotic zone that represented photosynthetically active tissues (Figure 6). As mentioned above, the canopy architectures of the three forest types can help explain why the distributions of FP and CHD in coniferous forests and mixed forests inclined to the under canopy, whereas the curves of broad-leaved forests were distributed more towards the middle or upper canopy (Figures 7 and 8b–d).

In general, due to a thinner upper canopy and dense under canopy for each forest type, the mean LAI increased rapidly and shifted to an infinitesimal increment from the ground up to the top of the canopy (Figure 8a). Below the threshold of 12 m (approximately middle canopy), dense foliage accumulated in the lower canopy of mixed forests and coniferous forests but mixed forests had more understory shrubs and slightly denser canopies than coniferous forests whereas broad-leaved forest had less shrubbery; therefore, there was a dramatically increased LAIc in mixed forests, followed by coniferous forests and broad-leaved forests. Along with still moderate density of foliage near the upper canopy in broad-leaved forests as well as thinned density of foliage in mixed forests and coniferous forests, the mean LAIc increased trend remained relatively stable in broad-leaved forests compared to other forest types. Eventually, broad-leaved forests had the highest mean LAIc, followed by mixed forests and coniferous forests, which is consistent with the findings of previous studies [80,81].

#### 4.2. Predictive Models

In comparison, the forest type-specific models had higher accuracies ( $Adj-R^2 = 0.44\text{--}0.88$ ,  $rRMSE = 5.13\text{--}28.42\%$ ) than the general models ( $Adj-R^2 = 0.39\text{--}0.77$ ,  $rRMSE = 8.54\text{--}29.86\%$ ). Bouvier et al. (2015) [14] developed a separate model for coniferous, deciduous and mixed stands to estimate forest structural parameters in the Lorraine forests. The results demonstrated that the separate models reduce estimation errors (2.0–5.3%) compared to general models in some complex forests conditions, which was confirmed by our research results. Fu et al. (2011) [82] reported  $R^2$  values for AGB of 0.37 of the general model and 0.43–0.68 of forest type-specific models in subtropical forests (located in southern Yunnan province, China). In our study site, the multi-layered forest conditions in subtropical forests contained greater species diversity, making the effects of tree-species composition (classified as forest types) significant. Overall, the models of the forest structural parameters were relatively more accurate for coniferous forests than broad-leaved forests and mixed forests. The relationships between stand structure and the forest structural parameters are species-dependent, and coniferous forests are usually characterized by relatively simple stand structures when compared with broad-leaved or mixed stands. So it is likely that the model prediction accuracy may decrease in multispecies stands [14]. Xu et al. (2015) [83] estimated forest structural parameters (i.e., Lorey's mean height, stem density, basal area and volume) in the subtropical deciduous mixed forests (on Purple Mountain, located in eastern Nanjing), using canopy height metrics (i.e., height percentile, mean height, maximum height and minimal height) and canopy density metrics. Compared with

our results ( $rRMSE = 5.13\text{--}22.28\%$ ), theirs showed a relatively lower  $rRMSE$  for Lorey's mean height (6.47%), stem density (27.04%), basal area (16.38%), and volume (6.93%). Compared with canopy metrics-based models ( $Adj-R^2 = 0.39\text{--}0.83$ ,  $rRMSE = 6.94\text{--}29.26\%$ ), standard metrics-based models had relatively higher performance ( $Adj-R^2 = 0.42\text{--}0.84$ ,  $rRMSE = 5.60\text{--}29.86\%$ ), except for the volume and AGB (both in forest type-specific models). The combination models performed best ( $Adj-R^2 = 0.45\text{--}0.88$ ,  $rRMSE = 5.13\text{--}28.96\%$ ), explaining a large amount of the variability for all forest structural parameters and indicating the increased utility of canopy metrics in capturing spatially explicit information describing a heterogeneous forest structure. For DBH, stem density, basal area, and AGB, Lefsky et al. (1999) [36] reported adjusted  $R^2$  values of 0.61, 0.52, 0.87, and 0.91 in boreal forests, markedly higher than reported in this study. The cause of the lower performance in this research is likely the complex structure of the subtropical forests, which are typified by multi-layered forests which encompass some stands with considerable variability in tree height and stem density, especially in old-growth stands, whereas boreal forests have a much higher homogeneous composition and more discernible canopy architecture.

When considering the selected frequency of metrics in the fitted models, for CV metrics, *Oligophotic*, *Empty* metrics were mostly selected by the combination models. This may be explained by the higher proportions of canopy elements (Figures 5 and 6), which were oligophotic, empty volume zones, revealing the strong sensitivity and representativeness of these two metrics to local forest structures. Previous studies [38,84] found that the Weibull scale and shape parameter were related to canopy attributes (e.g., crown depth and crown length), hence two Weibull parameters were both selected by the CM models of structural parameters (e.g., mean diameter, Lorey's mean height, basal area, and volume models) linked to canopy attributes. In combination models, the most selected WF metrics were  $\alpha_1$  and  $\beta_1$ , indicating that both of them are suitable for estimating structure parameters in local forests. The capacity of the Weibull parameters to represent the key attributes of mean crown dimension is important, as it provides a mechanism to summarize complex canopy characteristics into simple parameters that can be empirically analyzed in relation to various forest stand characteristics. The two-parameter Weibull model was applied for characterizing many types of FPs and CHDs in this study. In general, these profiles of single layer canopies corresponded well (Figure 7). However, the unimodal Weibull distribution function applied to the profile is inadequate to describe properly multimodal structure, which may occur in multi-layered, multi-age, complex forest stands [52]. Thus, the relatively poor fit for multi-layered forests could result in errors in estimates of structural parameters, which may explain why the Weibull parameters are not statistically more significant predictors than CV metrics. In this regard, future work could focus on how to apply a multi curve fitting approach in order to further capture the full distributions of canopy vertical profiles. On the other hand, different plot selection strategies could influence the performance of predictive models [85]. The plot selection in this study was only according to forest type, thus our future work could also examine different plot selection strategies of field training plots (e.g., using LiDAR data or geographical factors as a prior information, etc.) and utilize a suitable strategy to improve the estimation accuracy of forest structural parameters.

#### 4.3. The Selection of Voxel Sizes

Voxels representing canopy elements such as trunks and branches were abstracted by a volume grid and placed in a 3D grid [86]. As a method of volume visualization of LiDAR points, voxels have already been applied to airborne LiDAR data for improving calculations of forest attributes [87,88]. Voxel size is a key parameter pertaining to the scale of forest structural parameter estimates to the physical dimension of canopy components [89]. Thus, a sensitivity analysis was conducted to investigate the influence of various voxel sizes on forest structural estimations. As shown in Figure 10, in very low (i.e.,  $1 \times 1 \times 0.5 \text{ m}^3$ ) or high (i.e.,  $10 \times 10 \times 1 \text{ m}^3$ ) resolution conditions, the  $R^2$  values showed a relatively lower performance. If voxels are too small, a voxel-based CVM approach may produce redundant unfilled voxels of empty volume containing few tree canopy elements, which may

lead to the underestimation of forest structural parameters; however, too large voxels may lead to too few voxels and result in statistically insignificant descriptions of canopy features [90]. In these conditions, the voxel approach could become ineffective at characterizing the vertical distribution of various canopy structures and the capability to capture 3D heterogeneity of canopy structure for CV metrics could be constrained, hence resulting in relatively lower performances of the models. After taking into account factors of plot size ( $30 \times 30 \text{ m}^2$ ), point cloud densities ( $3.74 \text{ pts}\cdot\text{m}^{-2}$ ), etc., Hilker et al. (2010) [39] used a voxel size of  $6 \times 6 \times 1 \text{ m}^3$  for discrete airborne LiDAR data to estimate the tree height and LAI in Douglas-fir-dominated forest stands with relatively high tree heights (30–35 m). Concerning a much higher point cloud density ( $5.06 \text{ pts}\cdot\text{m}^{-2}$ ) of LiDAR data and relatively lower tree heights (4.47–18.52 m) in this study site, a 1 m vertical resolution produced more coarse data than the vertical resolution of 0.5 m (approximately treble the temporal sample spacing of 1 ns (15 cm)), thus, constraining the ability of canopy volume metrics to describe the vertical variability of the forest canopy structures. Moreover, potential tree movement due to wind between laser acquisitions is also considered a source of uncertainty, as laser returns from the same target can be located in different voxels for different laser acquisitions. By using a voxel size larger than the pulse diameter, this issue can be slightly reduced [91]. Overall, the optimal voxel size is a key parameter to determine in order to improve characterizations of forest structure [92,93]. Consequently, the optimal voxel spatial resolution should be determined based on plot size, the characteristics of the LiDAR instrument used (e.g., beam diameter, footprint size, average point density and temporal sample spacing, etc.), and forest structure attributes (e.g., tree height, crown diameter, crown depth, etc.)

## 5. Conclusions

In this study, a set of canopy metrics derived from canopy vertical profiles, which has the potential to aid in our understanding of the physical characteristics of forest structure, was extracted. The capability of the standard metrics (extracted from the point cloud data) and canopy metrics for estimating forest structural parameters (i.e., DBH, Lorey's mean height, stem density, basal area, volume, and AGB) was assessed, individually and in combination, over a subtropical forest in southeastern China. Moreover, a sensitive analysis of different voxel sizes was performed to investigate the optimal voxel size for estimating forest structural parameters.

The results demonstrated that the forest type-specific models had relatively higher accuracies ( $Adj-R^2 = 0.44\text{--}0.88$ ,  $rRMSE = 5.13\text{--}28.42\%$ ) compared with the general models ( $Adj-R^2 = 0.39\text{--}0.77$ ,  $rRMSE = 8.54\text{--}29.86\%$ ). The estimation accuracies of Lorey's mean height and AGB were the highest, followed by volume, DBH and basal area, whereas stem density was relatively lower. Overall, metrics of *Oligophotic*, *Empty*, *Open*,  $\alpha_1$  were the most frequently selected, indicating their potential capability for predicting forest structural parameters in the forest stands within the study site. The results demonstrated the synergistic use of standard metrics and canopy metrics for better predicting forest structural parameters ( $\Delta Adj-R^2 = 0.01\text{--}0.20$ ,  $\Delta rRMSE = -5.71\text{--}1.39\%$ ), compared with models developed using standard metrics (only) and canopy metrics (only). In addition, the optimal voxel size for estimating forest structural parameters in this study is  $5 \times 5 \times 0.5 \text{ m}^3$ , and the voxel vertical and horizontal resolutions should be determined based on plot size, the characteristics of the acquired LiDAR data (i.e., beam diameter, footprint size, average point density, and temporal sample spacing) and forest structure attributes (i.e., tree height, crown diameter, and crown depth).

**Acknowledgments:** The project was funded by the Natural Science Foundation of Jiangsu Province (No. BK20151515) and the National Natural Science Foundation of China (No. 31400492). This research was also supported by the Priority Academic Program Development of Jiangsu Higher Education Institutions (PAPD). Special thanks to Xin Shen, Kun Liu, and Ting Xu for field works. The authors gratefully acknowledge the foresters in Yushan forest for their assistance with data collection and sharing their rich knowledge and working experience of the local forest ecosystems.

**Author Contributions:** Zhengnan Zhang analyzed the data and wrote the paper. Lin Cao helped in project and study design, paper writing, and analysis. Guanghui She helped with data analysis and paper writing.

**Conflicts of Interest:** The authors declare no conflict of interest.

## Appendix A

**Table A1.** Allometric equations for aboveground biomass components of dominant tree species and species group in the study site.

Tree Species	Component	a	b	R <sup>2</sup>	References
Masson pine	Stem wood ( $W_s$ )	0.141	1.092	0.9970	Jiang et al. (1992) [42]
	Live branches ( $W_b$ )	0.065	0.991	0.9871	
	Foliage ( $W_f$ )	0.132	0.745	0.9827	
Chinese fir	Stem wood ( $W_s$ )	0.124	0.680	0.9704	Ye and Jiang (1983) [43]
	Live branches ( $W_b$ )	0.203	0.385	0.7223	
	Foliage ( $W_f$ )	0.850	0.189	0.6567	
Slash pine	Stem wood ( $W_s$ )	0.235	0.900	0.9523	Wang and Shi (1990) [44]
	Live branches ( $W_b$ )	0.080	1.064	0.8520	
	Foliage ( $W_f$ )	0.456	0.610	0.8802	
Sawtooth oak	Stem wood ( $W_s$ )	0.018	1.034	0.9864	Xu et al. (2011) [46]
	Live branches ( $W_b$ )	0.00008	1.468	0.9745	
	Foliage ( $W_f$ )	0.004	0.769	0.8662	
Sweet gum	Stem wood ( $W_s$ )	0.093	0.801	0.9310	Qian (2000) [45]
	Live branches ( $W_b$ )	0.083	0.649	0.9890	
	Foliage ( $W_f$ )	1.084	0.217	0.6940	
Other broadleaves <sup>a</sup>	Stem wood ( $W_s$ )	0.023	0.985	0.9903	Sun et al. (1992) [47]
	Live branches ( $W_b$ )	0.00004	3.785	0.9623	
	Foliage ( $W_f$ )	0.00003	1.378	0.9456	

Notes: The equation of  $W = a(D^2H)^b$  was used to calculate each biomass component.  $H$  = Tree height (m),  $D$  = DBH (cm) and  $a$ ,  $b$  are the parameters. <sup>a</sup> The general equation of “Other broadleaves” includes tree species of *Quercus variabilis*, *Quercus fabri*, *Quercus aliena*, *Quercus glandurifera* var. *brevipetiolata*, *Castanea sequinii*, *Liquidambar formosana* and *Pistacia chinensis*.

**Table A2.** Predictive models and accuracy assessment results (by standard metrics).

Variables	Predictive Models	Adj-R <sup>2</sup>	RMSE	rRMSE %
<i>All plots</i>				
DBH/cm	$\exp(1.064 + 0.641 \ln h_{95} - 0.580 \ln d_1 + 0.066 \ln d_7) \times 1.008$	0.60 ***	1.72	12.33
$h_{\text{Lorey}}/\text{m}$	$\exp(-0.33 - 0.079 \ln h_{\text{cv}} + 1.012 \ln h_{95} - 0.028 \ln d_7 - 0.001 \ln d_9) \times 1.006$	0.75 ***	0.97	9.15
$N/(\text{ha}^{-1})$	$\exp(6.814 - 0.049 \ln h_{\text{cv}} + 2.124 \ln d_1 - 0.296 \ln d_7 - 0.049 \ln d_9) \times 1.052$	0.42 ***	423.75	29.86
$G/(\text{m}^2 \cdot \text{ha}^{-1})$	$\exp(0.899 + 0.851 \ln h_{95} - 0.819 \ln d_3 - 0.177 \ln d_7) \times 1.019$	0.44 ***	3.99	17.23
$V/(\text{m}^3 \cdot \text{ha}^{-1})$	$\exp(3.445 - 0.137 \ln h_{\text{cv}} + 0.232 \ln h_{25} + 0.515 \ln h_{50} + 0.295 \ln d_3) \times 1.023$	0.46 ***	22.34	17.46
AGB/(Mg·ha <sup>-1</sup> )	$\exp(-0.169 - 0.058 \ln h_{\text{kurtosis}} + 1.817 \ln h_{95} + 0.627 \ln d_3 - 0.048 \ln d_9) \times 1.037$	0.64 ***	19.17	22.47
<i>Coniferous forests</i>				
DBH/cm	$\exp(0.996 + 0.664 \ln h_{95} - 0.485 \ln d_1 + 0.88 \ln d_7) \times 1.006$	0.67 **	1.20	9.50
$h_{\text{Lorey}}/\text{m}$	$\exp(-1.480 - 0.488 \ln h_{\text{cv}} + 1.211 \ln h_{95} - 0.102 \ln d_7 - 0.008 \ln d_9) \times 1.013$	0.66	1.09	11.47
$N/(\text{ha}^{-1})$	$\exp(6.39 - 0.851 \ln h_{\text{cv}} + 1.810 \ln d_1 - 0.477 \ln d_7 + 0.140 \ln d_9) \times 1.036$	0.60	315.78	18.68
$G/(\text{m}^2 \cdot \text{ha}^{-1})$	$\exp(-0.885 + 1.531 \ln h_{95} + 1.380 \ln d_3 - 0.376 \ln d_7) \times 1.029$	0.62 **	4.53	19.63
$V/(\text{m}^3 \cdot \text{ha}^{-1})$	$\exp(3.459 + 0.633 \ln h_{\text{cv}} + 3.732 \ln h_{25} - 2.335 \ln h_{50} + 0.491 \ln d_3) \times 1.029$	0.69 **	22.40	19.22
AGB/(Mg·ha <sup>-1</sup> )	$\exp(-2.216 + 0.565 \ln h_{\text{kurtosis}} + 2.218 \ln h_{95} + 0.455 \ln d_3 - 0.099 \ln d_9) \times 1.059$	0.72 **	16.86	24.17
<i>Broad-leaved forests</i>				
DBH/cm	$\exp(0.949 + 0.680 \ln h_{95} - 0.654 \ln d_1 + 0.028 \ln d_7) \times 1.009$	0.61 **	1.70	11.12
$h_{\text{Lorey}}/\text{m}$	$\exp(-0.296 - 0.149 \ln h_{\text{cv}} + 0.981 \ln h_{95} - 0.082 \ln d_7 - 0.031 \ln d_9) \times 1.004$	0.84 ***	0.78	6.91
$N/(\text{ha}^{-1})$	$\exp(7.663 + 0.602 \ln h_{\text{cv}} + 2.500 \ln d_1 - 0.144 \ln d_7 - 0.071 \ln d_9) \times 1.056$	0.60	298.99	26.55
$G/(\text{m}^2 \cdot \text{ha}^{-1})$	$\exp(3.045 + 0.046 \ln h_{95} + 0.516 \ln d_3 - 0.001 \ln d_7) \times 1.010$	0.54	2.62	11.96
$V/(\text{m}^3 \cdot \text{ha}^{-1})$	$\exp(3.459 + 0.633 \ln h_{\text{cv}} + 3.732 \ln h_{25} - 2.335 \ln h_{50} + 0.491 \ln d_3) \times 1.029$	0.56	19.49	14.68
AGB/(Mg·ha <sup>-1</sup> )	$\exp(1.958 - 0.060 \ln h_{\text{kurtosis}} + 1.150 \ln h_{95} + 0.579 \ln d_3 + 0.057 \ln d_9) \times 1.063$	0.57	26.80	28.42
<i>Mixed forests</i>				
DBH/cm	$\exp(1.184 + 0.360 \ln h_{95} - 1.116 \ln d_1 + 0.110 \ln d_7) \times 1.008$	0.48 **	1.66	11.94
$h_{\text{Lorey}}/\text{m}$	$\exp(0.830 + 0.222 \ln h_{\text{cv}} + 0.700 \ln h_{95} + 0.135 \ln d_7 - 0.067 \ln d_9) \times 1.003$	0.81 ***	0.60	5.60
$N/(\text{ha}^{-1})$	$\exp(7.774 + 0.093 \ln h_{\text{cv}} + 4.386 \ln d_1 - 0.391 \ln d_7 + 0.157 \ln d_9) \times 1.031$	0.48 **	336.73	28.52
$G/(\text{m}^2 \cdot \text{ha}^{-1})$	$\exp(1.308 + 0.772 \ln h_{95} + 1.036 \ln d_3 - 0.046 \ln d_7) \times 1.009$	0.45 **	3.08	12.86
$V/(\text{m}^3 \cdot \text{ha}^{-1})$	$\exp(3.144 + 0.006 \ln h_{\text{cv}} - 2.519 \ln h_{25} + 3.238 \ln h_{50} + 2.386 \ln d_3) \times 1.009$	0.60 ***	16.76	12.70
AGB/(Mg·ha <sup>-1</sup> )	$\exp(-0.177 - 0.261 \ln h_{\text{kurtosis}} + 1.917 \ln h_{95} + 1.380 \ln d_3 - 0.081 \ln d_9) \times 1.016$	0.64 ***	13.20	14.77

Notes: Level of significance: NS = not significant (>0.05); \*\* <0.01; \*\*\* <0.001.

**Table A3.** Predictive models and accuracy assessment results (by canopy metrics).

Variables	Predictive Models	Adj-R <sup>2</sup>	RMSE	rRMSE %
<i>All plots</i>				
DBH/cm	$\exp(2.852 + 0.169 \ln OG - 0.076 \ln Oligo + 0.081 \ln Empty - 0.576 \ln \beta_2) \times 1.010$	0.50 ***	1.86	13.31
$h_{Lorey}/m$	$\exp(-0.235 - 0.421 \ln Oligo + 1.010 \ln Filled - 0.272 \ln Empty - 0.338 \ln \beta_2) \times 1.009$	0.61 ***	1.18	11.13
$N/(ha^{-1})$	$\exp(5.545 - 0.508 \ln OG + 0.232 \ln Eu + 0.342 \ln Oligo + 1.332 \ln \beta_1) \times 1.055$	0.39 ***	415.17	29.26
$G/(m^2 \cdot ha^{-1})$	$\exp(2.119 + 0.579 \ln Oligo + 0.579 \ln Empty + 0.094 \ln \alpha_2) \times 1.020$	0.41 ***	3.67	15.82
$V/(m^3 \cdot ha^{-1})$	$\exp(3.063 + 0.249 \ln OG + 0.237 \ln Eu + 0.423 \ln Oligo - 0.694 \ln \alpha_1) \times 1.025$	0.42 ***	22.36	17.48
AGB/(Mg·ha <sup>-1</sup> )	$\exp(1.650 - 0.292 \ln OG + 1.021 \ln Oligo - 0.071 \ln CG + 0.717 \ln Empty) \times 1.048$	0.54 ***	19.84	23.25
<i>Coniferous forests</i>				
DBH/cm	$\exp(1.455 - 0.535 \ln OG + 0.388 \ln Oligo + 0.622 \ln Empty - 0.052 \ln \beta_2) \times 1.009$	0.54	1.40	11.09
$h_{Lorey}/m$	$\exp(-4.620 - 4.700 \ln Oligo + 5.948 \ln Filled + 0.281 \ln Empty - 2.952 \ln \beta_2) \times 1.014$	0.64	1.21	12.79
$N/(ha^{-1})$	$\exp(5.379 - 0.310 \ln OG - 0.726 \ln Eu + 1.019 \ln Oligo + 1.156 \ln \beta_1) \times 1.042$	0.58	431.65	25.53
$G/(m^2 \cdot ha^{-1})$	$\exp(-1.378 + 1.535 \ln Oligo + 0.195 \ln Empty - 2.715 \ln \alpha_2) \times 1.043$	0.55	4.73	20.48
$V/(m^3 \cdot ha^{-1})$	$\exp(-1.462 + 0.559 \ln OG + 2.869 \ln Eu - 0.765 \ln Oligo - 6.184 \ln \alpha_1) \times 1.028$	0.72 **	18.32	15.72
AGB/(Mg·ha <sup>-1</sup> )	$\exp(-3.600 - 3.719 \ln OG + 2.238 \ln Oligo - 1.604 \ln CG + 5.287 \ln Empty) \times 1.043$	0.74 **	18.51	26.55
<i>Broad-leaved forests</i>				
DBH/cm	$\exp(3.562 + 0.454 \ln OG - 0.053 \ln Oligo - 0.099 \ln Empty - 0.958 \ln \beta_2) \times 1.010$	0.51	1.81	11.79
$h_{Lorey}/m$	$\exp(1.030 - 0.149 \ln Oligo + 0.323 \ln Filled + 0.250 \ln Empty - 0.613 \ln \beta_2) \times 1.004$	0.83 ***	0.88	7.72
$N/(ha^{-1})$	$\exp(6.025 - 0.774 \ln OG + 1.103 \ln Eu - 0.015 \ln Oligo + 0.836 \ln \beta_1) \times 1.078$	0.52	299.82	26.63
$G/(m^2 \cdot ha^{-1})$	$\exp(2.514 + 0.321 \ln Oligo - 0.040 \ln Empty - 0.032 \ln \alpha_2) \times 1.013$	0.50	2.74	12.48
$V/(m^3 \cdot ha^{-1})$	$\exp(5.339 - 0.234 \ln OG - 0.981 \ln Eu + 0.588 \ln Oligo + 0.715 \ln \alpha_1) \times 1.013$	0.58	18.97	14.28
AGB/(Mg·ha <sup>-1</sup> )	$\exp(4.009 - 0.188 \ln OG + 0.440 \ln Oligo + 0.615 \ln CG - 0.517 \ln Empty) \times 1.055$	0.60	26.45	28.05
<i>Mixed forests</i>				
DBH/cm	$\exp(3.172 + 0.169 \ln OG + 0.060 \ln Oligo + 0.002 \ln Empty - 0.724 \ln \beta_2) \times 1.009$	0.48	1.78	12.79
$h_{Lorey}/m$	$\exp(0.481 + 0.318 \ln Oligo + 0.390 \ln Filled + 0.210 \ln Empty - 0.109 \ln \beta_2) \times 1.003$	0.75 ***	0.75	6.94
$N/(ha^{-1})$	$\exp(4.939 - 0.262 \ln OG - 0.997 \ln Eu + 0.965 \ln Oligo + 1.804 \ln \beta_1) \times 1.034$	0.44	324.73	22.68
$G/(m^2 \cdot ha^{-1})$	$\exp(1.909 + 0.626 \ln Oligo + 0.080 \ln Empty + 0.153 \ln \alpha_2) \times 1.009$	0.45 ***	3.12	13.01
$V/(m^3 \cdot ha^{-1})$	$\exp(-0.871 + 0.626 \ln OG + 0.080 \ln Eu + 0.088 \ln Oligo + 0.744 \ln \alpha_1) \times 1.008$	0.65 ***	16.31	12.36
AGB/(Mg·ha <sup>-1</sup> )	$\exp(1.848 + 0.087 \ln OG + 1.195 \ln Oligo + 0.087 \ln CG + 0.119 \ln Empty) \times 1.013$	0.71 ***	13.00	14.55

Notes: Level of significance: NS = not significant (&gt;0.05); \*\* &lt;0.01; \*\*\* &lt;0.001.

**Table A4.** Predictive models and accuracy assessment results (using both standard metrics and canopy metrics).

Variables	Predictive Models	Adj-R <sup>2</sup>	RMSE	rRMSE %
<i>All forests</i>				
DBH/cm	$\exp(0.802 - 0.060 \ln h_{cv} - 0.095 \ln h_{75} + 0.7401 \ln d_1 - 0.548 \ln Oligo) \times 1.008$	0.61 ***	1.67	11.97
$h_{Lorey}/m$	$\exp(0.091 - 0.053 \ln h_{50} + 0.154 \ln d_1 + 0.971 \ln Empty - 0.315 \ln \beta_1) \times 1.009$	0.77 ***	0.90	8.54
$N/(ha^{-1})$	$\exp(7.012 + 0.167 \ln d_1 + 0.761 \ln Oligo + 0.741 \ln \alpha_1 + 1.643 \ln \beta_1) \times 1.049$	0.45 ***	410.02	28.90
$G/(m^2 \cdot ha^{-1})$	$\exp(1.576 - 0.255 h_{kurtosis} - 0.304 \ln h_{25} + 1.031 \ln h_{95} + 0.073 \ln Empty) \times 1.017$	0.50 ***	3.47	14.96
$V/(m^3 \cdot ha^{-1})$	$\exp(0.201 - 0.463 h_{75} - 0.502 \ln Oligo + 0.845 \ln Empty + 2.343 \ln \alpha_1) \times 1.018$	0.58 ***	21.07	16.47
AGB/(Mg·ha <sup>-1</sup> )	$\exp(0.519 + 0.193 \ln h_{95} + 1.458 \ln d_3 + 1.300 \ln CC_{2m} - 1.348 \ln Oligo) \times 1.036$	0.65 ***	18.25	21.39
<i>Coniferous forests</i>				
DBH/cm	$\exp(1.041 - 0.164 \ln h_{cv} + 0.062 \ln h_{75} + 0.8131 \ln d_1 - 0.182 \ln Oligo) \times 1.006$	0.74 **	1.08	8.59
$h_{Lorey}/m$	$\exp(-1.207 - 0.196 \ln h_{50} + 0.582 \ln d_1 + 1.441 \ln Empty - 0.661 \ln \beta_1) \times 1.010$	0.77**	0.99	10.43
$N/(ha^{-1})$	$\exp(1.881 + 0.573 \ln d_1 - 3.703 \ln Oligo + 2.036 \ln \alpha_1 + 0.029 \ln \beta_1) \times 1.033$	0.64	339.29	20.07
$G/(m^2 \cdot ha^{-1})$	$\exp(0.242 - 0.323 h_{kurtosis} - 0.060 \ln h_{25} + 1.668 \ln h_{95} + 0.046 \ln Empty) \times 1.029$	0.69 **	4.23	18.32
$V/(m^3 \cdot ha^{-1})$	$\exp(-1.585 - 0.537 h_{75} - 0.599 \ln Oligo + 1.392 \ln Empty + 3.014 \ln \alpha_1) \times 1.024$	0.78 **	18.21	15.63
AGB/(Mg·ha <sup>-1</sup> )	$\exp(-0.808 + 0.794 \ln h_{95} + 1.594 \ln d_3 + 3.551 \ln CC_{2m} - 4.560 \ln Oligo) \times 1.040$	0.81 **	14.53	20.83
<i>Broad-leaved forests</i>				
DBH/cm	$\exp(0.876 - 0.095 \ln h_{cv} - 0.325 \ln h_{75} + 0.5881 \ln d_1 - 0.797 \ln Oligo) \times 1.008$	0.68	1.54	10.06
$h_{Lorey}/m$	$\exp(1.020 + 0.047 \ln h_{50} - 0.226 \ln d_1 + 0.633 \ln Empty - 0.255 \ln \beta_1) \times 1.003$	0.88 ***	0.72	6.39
$N/(ha^{-1})$	$\exp(7.281 + 0.074 \ln d_1 + 0.8081 \ln Oligo + 0.583 \ln \alpha_1 + 2.132 \ln \beta_1) \times 1.055$	0.62	273.49	24.29
$G/(m^2 \cdot ha^{-1})$	$\exp(3.404 - 0.100 h_{kurtosis} - 0.166 \ln h_{25} + 1.109 \ln h_{95} - 0.902 \ln Empty) \times 1.009$	0.63	2.49	11.34
$V/(m^3 \cdot ha^{-1})$	$\exp(9.533 + 2.028 h_{75} + 1.027 \ln Oligo - 1.599 \ln Empty - 3.683 \ln \alpha_1) \times 1.011$	0.67	16.65	12.54
AGB/(Mg·ha <sup>-1</sup> )	$\exp(2.376 - 0.395 \ln h_{95} + 1.210 \ln d_3 + 3.440 \ln CC_{2m} - 4.200 \ln Oligo) \times 1.051$	0.66	26.67	28.29
<i>Mixed forests</i>				
DBH/cm	$\exp(0.615 + 0.012 \ln h_{cv} - 0.331 \ln h_{75} + 0.5901 \ln d_1 - 1.911 \ln Oligo) \times 1.008$	0.55 **	1.58	11.34
$h_{Lorey}/m$	$\exp(0.089 - 0.136 \ln h_{50} + 0.295 \ln d_1 + 1.043 \ln Empty - 0.969 \ln \beta_1) \times 1.002$	0.84 ***	0.55	5.13
$N/(ha^{-1})$	$\exp(8.121 + 0.135 \ln d_1 + 1.246 \ln Oligo + 0.120 \ln \alpha_1 + 4.921 \ln \beta_1) \times 1.029$	0.50 ***	319.05	22.28
$G/(m^2 \cdot ha^{-1})$	$\exp(-0.179 - 0.069 h_{kurtosis} + 0.361 \ln h_{25} - 1.140 \ln h_{95} + 1.927 \ln Empty) \times 1.009$	0.56 **	2.77	11.56
$V/(m^3 \cdot ha^{-1})$	$\exp(0.201 - 0.463 h_{75} - 0.502 \ln Oligo + 0.845 \ln Empty + 2.343 \ln \alpha_1) \times 1.018$	0.71 ***	15.87	12.02
AGB/(Mg·ha <sup>-1</sup> )	$\exp(0.519 + 0.630 \ln h_{95} + 1.113 \ln d_3 + 0.073 \ln CC_{2m} + 1.788 \ln Oligo) \times 1.009$	0.79 ***	10.89	12.19

Notes: Level of significance: NS = not significant (&gt;0.05); \*\* &lt;0.01; \*\*\* &lt;0.001.

## References

- Pan, Y.; Birdsey, R.A.; Phillips, O.L.; Jackson, R.B. The Structure, Distribution, and Biomass of the World's Forests. *Ann. Rev. Ecol. Evol. Syst.* **2013**, *44*, 593–622. [[CrossRef](#)]
- Hill, S.; Lati, H.; Heurich, M.; Müller, J. Individual-tree-and stand-based development following natural disturbance in a heterogeneously structured forest: A LiDAR-based approach. *Ecol. Inform.* **2017**, *38*, 12–25. [[CrossRef](#)]
- Franklin, J.F.; Spies, T.A.; Pelt, R.V.; Carey, A.B.; Thornburgh, D.A.; Rae, D.; Lindenmayer, D.B.; Harmon, M.E.; Keeton, W.S.; Shaw, D.C.; et al. Disturbances and structural development of natural forest ecosystems with silvicultural implications, using Douglas-fir forests as an example. *For. Ecol. Manag.* **2002**, *155*, 399–423. [[CrossRef](#)]
- Palace, M.W.; Sullivan, F.B.; Ducey, M.J.; Treuhaft, R.N.; Herrick, C.; Shimbo, J.Z.; Mota-E-Silva, J. Estimating forest structure in a tropical forest using field measurements, a synthetic model and discrete return lidar data. *Remote Sens. Environ.* **2015**, *161*, 1–11. [[CrossRef](#)]
- McElhinny, C.; Gibbons, P.; Brack, C.; Bauhus, J. Forest and woodland stand structural complexity: Its definition and measurement. *For. Ecol. Manag.* **2005**, *218*, 1–24. [[CrossRef](#)]
- Spies, T.A. Forest Structure: A Key to the Ecosystem. *Northwest Sci.* **1998**, *72*, 34–39.
- Zimble, D.A.; Evans, D.L.; Carlson, G.C.; Parker, R.C.; Grado, S.C.; Gerard, P.D. Characterizing vertical forest structure using small-footprint airborne LiDAR. *Remote Sens. Environ.* **2003**, *87*, 171–182. [[CrossRef](#)]
- Miura, N.; Jones, S.D. Characterizing forest ecological structure using pulse types and heights of airborne laser scanning. *Remote Sens. Environ. J.* **2010**, *114*, 1069–1076. [[CrossRef](#)]
- Pasher, J.; King, D.J. Multivariate forest structure modelling and mapping using high resolution airborne imagery and topographic information. *Remote Sens. Environ.* **2010**, *114*, 1718–1732. [[CrossRef](#)]
- Corlett, R.T. Where are the Subtropics? *Biotropica* **2013**, *45*, 273–275. [[CrossRef](#)]
- Zhang, Y.J.; Cristiano, P.M.; Zhang, Y.F.; Campanello, P.I.; Tan, Z.H.; Zhang, Y.P.; Goldstein, G.; Cao, K.F. Carbon Economy of Subtropical Forests. *Trop. Tree Physiol.* **2016**, *6*, 337–355.
- Global Forest Resources Assessment 2015. Available online: <http://www.fao.org/3/a-i4808e.pdf> (accessed on 14 June 2017).
- Ouyang, S.; Xiang, W.; Wang, X.; Zeng, Y.; Lei, P.; Deng, X.; Peng, C. Significant effects of biodiversity on forest biomass during the succession of subtropical forest in south China. *For. Ecol. Manag.* **2016**, *372*, 291–302. [[CrossRef](#)]
- Bouvier, M.; De, M.; Renaud, J. Generalizing predictive models of forest inventory attributes using an area-based approach with airborne LiDAR data area-based approach with airborne LiDAR data. *Remote Sens. Environ.* **2015**, *156*, 322–334. [[CrossRef](#)]
- White, J.C.; Coops, N.C.; Wulder, M.A.; Vastaranta, M.; Hilker, T.; Tompalski, P.; White, J.C.; Coops, N.C.; Wulder, M.A.; Vastaranta, M.; et al. Remote Sensing Technologies for Enhancing Forest Inventories: A Review Remote Sensing Technologies for Enhancing Forest Inventories: A Review. *Can. J. Remote Sens.* **2016**, *42*, 619–641. [[CrossRef](#)]
- Mcroberts, R.E.; Tomppo, E.O. Remote sensing support for national forest inventories. *Remote Sens. Environ.* **2007**, *110*, 412–419. [[CrossRef](#)]
- Wulder, M.A.; White, J.C.; Nelson, R.F.; Næsset, E.; Ørka, H.O.; Coops, N.C.; Hilker, T.; Bater, C.W.; Gobakken, T. Lidar sampling for large-area forest characterization: A review. *Remote Sens. Environ.* **2012**, *121*, 196–209. [[CrossRef](#)]
- Wulder, M. Optical remote-sensing techniques for the assessment of forest inventory and biophysical parameters. *Prog. Phys. Geogr.* **1998**, *22*, 449–476. [[CrossRef](#)]
- Duncanson, L.I.; Niemann, K.O.; Wulder, M.A. Integration of GLAS and Landsat TM data for aboveground biomass estimation. *Carbon* **2010**, *36*, 129–141. [[CrossRef](#)]
- Lu, D.; Chen, Q.; Wang, G.; Moran, E.; Batistella, M.; Zhang, M.; Laurin, G.V.; Saah, D. Aboveground Forest Biomass Estimation with Landsat and LiDAR Data and Uncertainty Analysis of the Estimates. *Int. J. For. Res.* **2012**, *2012*. [[CrossRef](#)]
- Rosenqvist, Å.; Milne, A.; Lucas, R.; Imhoff, M.; Dobson, C. A review of remote sensing technology in support of the Kyoto Protocol. *Environ. Sci. Policy* **2003**, *6*, 441–455. [[CrossRef](#)]

22. Yu, Y.; Yang, X.; Fan, W. Estimates of forest structure parameters from GLAS data and multi-angle imaging spectrometer data. *Int. J. Appl. Earth Obs. Geoinf.* **2015**, *38*, 65–71. [[CrossRef](#)]
23. Li, W.; Niu, Z.; Chen, H.; Li, D.; Wu, M.; Zhao, W. Remote estimation of canopy height and aboveground biomass of maize using high-resolution stereo images from a low-cost unmanned aerial vehicle system. *Ecol. Indic.* **2016**, *67*, 637–648. [[CrossRef](#)]
24. Véga, C.; Renaud, J.; Durrieu, S.; Bouvier, M. On the interest of penetration depth, canopy area and volume metrics to improve Lidar-based models of forest parameters. *Remote Sens. Environ.* **2016**, *175*, 32–42. [[CrossRef](#)]
25. Means, J.E.; Acker, S.A.; Fitt, B.J.; Renslow, M.; Emerson, L.; Abstract, C.J.H. Predicting Forest Stand Characteristics with Airborne Scanning Lidar. *Photogramm. Eng. Remote Sens.* **2000**, *66*, 1367–1371.
26. Silva, C.A.; Klauber, C.; Hudak, A.T.; Vierling, L.A.; Liesenberg, V.; Carvalho, S.P.C.E.; Rodriguez, L.C.E. A principal component approach for predicting the stem volume in Eucalyptus plantations in Brazil using airborne LiDAR data. *Forestry* **2016**, *89*, 422–433. [[CrossRef](#)]
27. Tesfamichael, S.G.; Beech, C. Combining Akaike's Information Criterion and discrete return LiDAR data to estimate structural attributes of savanna woody vegetation. *J. Arid Environ.* **2016**, *129*, 25–34. [[CrossRef](#)]
28. Sabol, J.; Procházka, D.; Patočka, Z. Development of models for forest variable estimation from airborne laser scanning data using an area-based approach at a plot level. *J. For. Sci.* **2016**, *62*, 137–142. [[CrossRef](#)]
29. Frazer, G.W.; Magnussen, S.; Wulder, M.A.; Niemann, K.O. Simulated impact of sample plot size and co-registration error on the accuracy and uncertainty of LiDAR-derived estimates of forest stand biomass. *Remote Sens. Environ. J.* **2011**, *115*, 636–649. [[CrossRef](#)]
30. Montealegre, A.L.; Riva, J.D.; García-martín, A. Use of low point density ALS data to estimate stand-level structural variables in Mediterranean Aleppo pine forest. *Forestry* **2016**, 1–10. [[CrossRef](#)]
31. Zolkos, S.G.; Goetz, S.J.; Dubayah, R. A meta-analysis of terrestrial aboveground biomass estimation using lidar remote sensing. *Remote Sens. Environ.* **2013**, *128*, 289–298. [[CrossRef](#)]
32. Magnussen, S.; Næsset, E.; Gobakken, T. Reliability of LiDAR derived predictors of forest inventory attributes: A case study with Norway spruce. *Remote Sens. Environ.* **2010**, *114*, 700–712. [[CrossRef](#)]
33. Magnussen, S.; Næsset, E.; Gobakken, T. Prediction of tree-size distributions and inventory variables from cumulants of canopy height distributions. *Forestry* **2013**, *86*, 583–595. [[CrossRef](#)]
34. MacArthur, R.; MacArthur, J.W. On bird species diversity. *Ecology* **1961**, *42*, 594–598.
35. Aber, J.D. A method for estimating foliage-height profiles in broad-leaved forests. *Ecology* **1979**, *67*, 35–40. [[CrossRef](#)]
36. Lefsky, M.A.; Cohen, W.B.; Acker, S.A.; Parker, G.G. Lidar Remote Sensing of the Canopy Structure and Biophysical Properties of Douglas-Fir Western Hemlock Forests. *Remote Sens. Environ.* **1999**, *361*, 339–361. [[CrossRef](#)]
37. Lovell, J.L.; Jupp, D.L.B.; Culvenor, D.S.; Coops, N.C.; Les, R. Using airborne and ground-based ranging lidar to measure canopy structure in Australian forests. *Can. J. Remote Sens.* **2003**, *29*, 607–622. [[CrossRef](#)]
38. Coops, N.C.; Hilker, T.; Wulder, M.A.; St-Onge, B.; Newnham, G.; Siggins, A.; Trofymow, J.A. Estimating canopy structure of Douglas-fir forest stands from discrete-return LiDAR. *Trees* **2007**, *21*, 295–310. [[CrossRef](#)]
39. Hilker, T.; Leeuwen, M.V.; Coops, N.C. Comparing canopy metrics derived from terrestrial and airborne laser scanning in a Douglas-fir dominated forest stand. *Trees* **2010**, *24*, 819–832. [[CrossRef](#)]
40. Kraus, K.; Pfeifer, N. Determination of terrain models in wooded areas with airborne laser scanner data. *ISPRS J. Photogramm. Remote Sens.* **1998**, *53*, 193–203. [[CrossRef](#)]
41. Song, Y.B.; Ding, Y.P. The development and latest progress of JSCORS. *Bull. Surv. Mapp.* **2009**, *2*, 73–74.
42. Jiang, B.; Yuan, W.; Zhu, G. A preliminary study on the plantation biomass and produce structure of *Pinus massoniana*, *Pinus elliotii* and *Pinus taeda*. *J. Zhejiang For. Sci. Technol.* **1992**, *12*, 1–9.
43. Ye, J.; Yang, Z. Biomass structure of planted Chinese fir in Southern Jiangsu province, China. *Acta Ecol. Sin.* **1983**, *3*, 7–14.
44. Wang, Q.; Shi, Y. A preliminary study on the biomass and production of slash pine plantation in Jiangsu province. *Acta Phytoecol. Geobot. Sin.* **1990**, *14*, 2–12.
45. Xu, J.; Wang, M.; Huang, Q.; Gong, S. Study on aboveground biomass model of natural individual trees of *Quercus acutissima*. *Anhui For. Sci. Technol.* **2011**, *37*, 3–6.
46. Qian, G. Studies on the dynamic change of the net production quantity of liquidambar formosana plantation. *Acta Agric. Univ. Jiangxiensis* **2000**, *22*, 399–404.

47. Sun, D.; Ruan, H.; Ye, J. Biomass Structure of Oak-Dominated Secondary Forest in Kongqingshan. Available online: [http://refhub.elsevier.com/S0034-4257\(16\)30106-7/rf0260](http://refhub.elsevier.com/S0034-4257(16)30106-7/rf0260) (accessed on 14 June 2017).
48. Zhao, K.; Popescu, S.; Nelson, R. Lidar remote sensing of forest biomass: A scale-invariant estimation approach using airborne lasers. *Remote Sens. Environ.* **2009**, *113*, 182–196. [[CrossRef](#)]
49. Weishampel, J.F.; Drake, J.B.; Cooper, A.; Blair, J.B.; Hofton, M. Forest canopy recovery from the 1938 hurricane and subsequent salvage damage measured with airborne LiDAR. *Remote Sens. Environ.* **2007**, *109*, 142–153. [[CrossRef](#)]
50. Bailey, R.; Dell, T. Quantifying diameter distributions with the Weibull function. *For. Sci.* **1973**, *19*, 97–104.
51. Penner, M.; Woods, M.; Pitt, D.G. A comparison of airborne laser scanning and image point cloud derived tree size class distribution models in Boreal Ontario. *Forests* **2015**, *6*, 4034–4054. [[CrossRef](#)]
52. Tompalski, P.; Coops, N.C.; White, J.C.; Wulder, M.A. Enriching ALS-derived area-based estimates of volume through tree-level downscaling. *Forests* **2015**, *6*, 2608–2630. [[CrossRef](#)]
53. Zhao, J.; Li, J.; Liu, Q. Review of forest vertical structure parameter inversion based on remote sensing technology. *J. Remote Sens.* **2013**, *17*, 697.
54. Jupp, D.L.B.; Culvenor, D.S.; Lovell, J.L.; Newnham, G.J.; Strahler, A.H.; Woodcock, C.E. Estimating forest LAI profiles and structural parameters using a ground-based laser called ‘Echidna<sup>®</sup>’. *Tree Physiol.* **2008**, *29*, 171–181. [[CrossRef](#)] [[PubMed](#)]
55. Hilker, T.; Coops, N.C.; Newnham, G.J.; Leeuwen, M.V.; Wulder, M.A.; Stewart, J.; Culvenor, D.S. Comparison of Terrestrial and Airborne LiDAR in Describing Stand Structure of a Thinned Lodgepole Pine Forest. *J. For.* **2012**, *10*, 97–104.
56. Sprugel, D. Correcting for Bias in Log-Transformed Allometric Equations. *Ecology* **1983**, *64*, 209–210. [[CrossRef](#)]
57. Næsset, E. Predicting forest stand characteristics with airborne scanning laser using a practical two-stage procedure and field data. *Remote Sens. Environ.* **2002**, *80*, 88–99. [[CrossRef](#)]
58. Næsset, E.; Bollandsås, O.M.; Gobakken, T. Comparing regression methods in estimation of biophysical properties of forest stands from two different inventories using laser scanner data. *Remote Sens. Environ.* **2005**, *94*, 541–553. [[CrossRef](#)]
59. García-gutiérrez, J.; Martínez-Álvarez, F.; Troncoso, A.; Riquelme, J.C. A comparison of machine learning regression techniques for LiDAR-derived estimation of forest variables. *Neurocomputing* **2015**, *167*, 24–31. [[CrossRef](#)]
60. Næsset, E.; Okland, T. Estimating tree height and tree crown properties using airborne scanning laser in a boreal. *Remote Sens. Environ.* **2002**, *79*, 105–115. [[CrossRef](#)]
61. Akaike, H. A new look at the statistical model identification. *IEEE Trans. Autom. Control* **1974**, *19*, 716–723. [[CrossRef](#)]
62. Kutner, M.; Nachtsheim, C.; Neter, J.; Li, W. *Applied Linear Statistical Models*, 5th ed.; McGraw-Hill/Irwin: New York, NY, USA, 2004.
63. Bengio, Y. No Unbiased Estimator of the Variance of K-Fold Cross-Validation. *J. Mach. Learn. Res.* **2004**, *5*, 1089–1105.
64. Parker, G.G. Structure and Microclimate of Forest Canopies. In *Forest Canopies*; Lowman, M.D., Nadkarni, N.M., Eds.; Academic Press: San Diego, CA, USA, 1995; pp. 73–106.
65. Wilkes, P.; Suarez, L.; Andrew, H.; Andrew, M.; William, W.; Mariela, S.-B.; Skidmore, A.K. Using discrete-return ALS to quantify number of canopy strata across diverse forest types Using discrete-return airborne laser scanning to quantify number of canopy strata across diverse forest types. *Methods Ecol. Evol.* **2015**, 1–13. [[CrossRef](#)]
66. Lefsky, M.A.; Harding, D.; Cohen, W.B.; Parker, G.; Shugart, H.H. Surface Lidar Remote Sensing of Basal Area and Biomass in Deciduous Forests of Eastern Maryland, USA. *Remote Sens. Environ.* **1999**, *67*, 83–98. [[CrossRef](#)]
67. Leiterer, R.; Torabzadeh, H.; Furrer, R.; Schaepman, M.E.; Morsdorf, F. Towards Automated Characterization of Canopy Layering in Mixed Temperate Forests Using Airborne Laser Scanning. *Forests* **2015**, *6*, 4146–4167. [[CrossRef](#)]
68. Van Leeuwen, M.; Nieuwenhuis, M. Retrieval of forest structural parameters using LiDAR remote sensing. *Eur. J. For. Res.* **2010**, *129*, 749–770. [[CrossRef](#)]

69. Ishii, H. The role of crown architecture, leaf phenology and photosynthetic activity in promoting complementary use of light among coexisting species in temperate forests. *Ecol. Res.* **2010**, *25*, 715–722. [[CrossRef](#)]
70. He, J.; Zhu, S. The Preliminary Study on the Law of the Crown Structure of Massons Pine in Mid-Subtropical Region. *J. Mt. Agric. Biol.* **1990**, *9*, 61–72.
71. Liang, X.; Ye, W. Advances in Study of Forest Gaps. *J. Trop. Subtrop. Bot.* **2001**, *9*, 355–364.
72. Kneeshaw, D.D.; Bergeron, Y. Canopy Gap Characteristics and Tree Replacement in the Southeastern Boreal Forest. *Ecology* **1998**, *79*, 783–794. [[CrossRef](#)]
73. An, S.; Zhao, R. Analysis of Characteristics of Secondary Forest Vegetation in the North Subtropical Zone of China. *J. Nanjing Univ. Sci.* **1991**, *27*, 324–331.
74. Spies, T.A.; Frankli, J.F. Gap Characteristics and Vegetation Response in Coniferous Forests of the Pacific Northwest. *Ecology* **1989**, *70*, 543–545. [[CrossRef](#)]
75. Yang, J.; Liu, X.; Yang, X. Forest canopy structure, light environment and their effects on the vegetation pattern and growth of understory in forests. *J. Sci. Teach. Univ.* **2015**, *35*, 57–62.
76. Montgomery, R.A.; Chazdon, R.L. Forest structure, canopy architecture, and light transmittance in old-growth and second-growth tropical rain forests. *Ecology* **2001**, *82*, 2707–2718. [[CrossRef](#)]
77. Zhu, S.; He, J. The Preliminary Study on the Law of the Crown Structure of Masson's pine in South-subtropical. *J. Mt. Agric. Biol.* **1993**, *12*, 36–44.
78. Messier, C.; Sylvain, P.; Bergeron, Y. Effects of Overstory and Understory Vegetation on the Understory Light Environment in Mixed Boreal Forests. *J. Veg. Sci.* **1998**, *9*, 511–520. [[CrossRef](#)]
79. Parent, S.; Messier, C. A simple and efficient method to estimate microsite light availability under a forest canopy. *Can. J. For. Res.* **1996**, *26*, 151–154. [[CrossRef](#)]
80. Zhao, F.; Yang, X.; Schull, M.A.; Román-colón, M.O.; Yao, T.; Wang, Z.; Zhang, Q.; Jupp, D.L.B.; Lovell, J.L.; Culvenor, D.S.; et al. Measuring effective leaf area index, foliage profile, and stand height in New England forest stands using a full-waveform ground-based lidar. *Remote Sens. Environ.* **2011**, *115*, 2954–2964. [[CrossRef](#)]
81. Tang, H.; Dubayah, R.; Brogly, M.; Ganguly, S.; Zhang, G. Large-scale retrieval of leaf area index and vertical foliage profile from the spaceborne waveform lidar (GLAS/ICESat). *Remote Sens. Environ.* **2014**, *154*, 8–18. [[CrossRef](#)]
82. Fu, T.; Pang, Y.; Huang, Q.F.; Liu, Q.W.; Xu, G.C. Prediction of Subtropical Forest Parameters Using Airborne Laser Scanner. *J. Remote Sens.* **2011**, *15*, 1092–1104.
83. Xu, Z.; Cao, L.; Ruan, H.; Li, W.; Jiang, S. Inversion of subtropical forest stand characteristics by integrating very high resolution imagery acquired from UAV and LiDAR point-cloud. *Chin. J. Plant Ecol.* **2015**, *39*, 849–856.
84. Wilkes, P.; Jones, S.; Suarez, L.; Haywood, A.; Mellora, A.; Soto-Berelov, M.; Woodgate, W. MAUP and LiDAR derived canopy structure. *Int. Geosci. Remote Sens. Symp.* **2013**, 173–175.
85. Maltamo, M.; Bollandsås, O.M.; Næsset, E.; Gobakken, T.; Packalén, P. Different plot selection strategies for field training data in ALS-assisted forest inventory. *Forestry* **2011**, *84*, 23–31. [[CrossRef](#)]
86. Van der Zande, D.; Stuckens, J.; Verstraeten, W.W.; Mereu, S.; Muys, B.; Coppin, P. 3D modeling of light interception in heterogeneous forest canopies using ground-based LiDAR data. *Int. J. Appl. Earth Obs. Geoinf.* **2011**, *13*, 792–800. [[CrossRef](#)]
87. Stoker, J. Volumetric Visualization of multiple-return Lidar Data: Using Voxels. *Photogramm. Eng. Remote Sens.* **2009**, *75*, 109–112.
88. Zheng, G.; Moskal, L.M. Computational-Geometry-Based Retrieval of Computational-Geometry-Based Retrieval of Effective Leaf Area Index Using Terrestrial Laser Scanning. *IEEE Geosci. Remote Sens. Soc.* **2015**, *50*, 3958–3969. [[CrossRef](#)]
89. Grau, E.; Durrieu, S.; Fournier, R.; Gastellu-etchegorry, J.; Yin, T. Estimation of 3D vegetation density with Terrestrial Laser Scanning data using voxels. A sensitivity analysis of influencing parameters. *Remote Sens. Environ.* **2017**, *191*, 373–388. [[CrossRef](#)]
90. Li, J.; Hu, B.; Noland, T.L. Classification of tree species based on structural features derived from high density LiDAR data. *Agric. For. Meteorol.* **2013**, *171–172*, 104–114. [[CrossRef](#)]

91. Kükenbrink, D.; Schneider, F.D.; Leiterer, R.; Schaepman, M.E.; Morsdorf, F. Quantification of hidden canopy volume of airborne laser scanning data using a voxel traversal algorithm. *Remote Sens. Environ.* **2017**, *194*, 424–436. [[CrossRef](#)]
92. Oshio, H.; Asawa, T.; Hoyano, A.; Miyasaka, S. Estimation of the leaf area density distribution of individual trees using high-resolution and multi-return airborne LiDAR data. *Remote Sens. Environ.* **2015**, *166*, 116–125. [[CrossRef](#)]
93. Béland, M.; Widlowski, J.; Fournier, R.A. A model for deriving voxel-level tree leaf area density estimates from ground-based LiDAR. *Environ. Model. Softw.* **2014**, *51*, 184–189. [[CrossRef](#)]



© 2017 by the authors. Licensee MDPI, Basel, Switzerland. This article is an open access article distributed under the terms and conditions of the Creative Commons Attribution (CC BY) license (<http://creativecommons.org/licenses/by/4.0/>).